

Reproducing Acceleration Power Spectral Density from an  
Aircraft Fuselage Panel excited by Turbulent Boundary Layer  
using Piezoelectric Actuators

by

Steven Albert James Sonnenberg

A thesis submitted to the Faculty of Graduate and Postdoctoral Affairs in  
partial fulfillment of the requirements for the degree of

Master of Applied Science

in

Aerospace Engineering

Carleton University  
Ottawa, Ontario

© 2017, Steven Albert James Sonnenberg

## **Abstract**

Noise and vibration in an aircraft cabin during cruise conditions is predominantly caused by external flow excitations from the turbulent boundary layer. The turbulent boundary layer causes the fuselage panels on the aircraft to vibrate. These vibrations radiate sound energy in the form of noise. This thesis describes a method to analytically optimize aircraft's cabin panel parameters, to reduce the acceleration power spectral density of the panel caused by the turbulent boundary layer, thereby reducing the radiated sound power into the cabin. In addition, this thesis presents an experimental validation, and modification of two existing analytical models used to calculate acceleration power spectral density for an aircraft panel, with three different excitations: (1) an impact hammer force, (2) a turbulent boundary layer, and (3) a piezoelectric patch. Finally, an optimization method has been developed to reproduce the acceleration power spectral density of an aircraft panel, at constant cruise conditions, by optimally selecting the placement of a given number of piezoelectric actuators, excited with a white noise distribution of frequencies within the human hearing range.

## **Acknowledgements**

I would like to start by thanking my supervisor, Professor Joana Rocha for all of her guidance and support throughout the past two years. I would like to thank her for helping me to go to Germany on an internship to help further the experimental research and open my eyes to the many possible directions my work may take me. I would also like to thank the other researchers, past and present, working under the supervision of Professor Rocha, for your suggestions and friendship.

I would like to thank Dr. Malte Misol, from DLR, for the support and guidance you provided me during my 4 months in Germany. It was a life changing experience.

I would like to thank Kelly Barker for being the love of my life and helping me get through every challenge and tough decision that I had to make. Also, thank you for always correcting my assignments. You always make me sound like a better writer than I am, so thank you.

I would like to thank Darren and Elaine Sonnenberg, for believing in me and always being there for me, you are the best parents anyone could ever ask for.

I would like to thank Dr. Jessica Sonnenberg for always encouraging me to set and attain higher goals. You have always been my role model and I will always look up to you and your accomplishments.

Finally, I would like to thank all my family and friends who have been there to support me in my pursuits. I never would have made it here if it weren't for all of you.

# Table of Contents

<b>Abstract</b> .....	<b>i</b>
<b>Acknowledgements</b> .....	<b>ii</b>
<b>Table of Contents</b> .....	<b>iii</b>
<b>List of Tables</b> .....	<b>v</b>
<b>List of Figures</b> .....	<b>vi</b>
<b>List of Appendices</b> .....	<b>x</b>
<b>List of Abbreviations</b> .....	<b>xi</b>
<b>Nomenclature</b> .....	<b>xii</b>
<b>Chapter 1: Introduction</b> .....	<b>1</b>
1.1 Objective.....	1
1.2 Motivation .....	1
1.3 Contributions to State of the Art.....	3
<b>Chapter 2: Literature Review</b> .....	<b>5</b>
2.1 Acceleration Power Spectral Density and Radiated Sound Power.....	5
2.2 Piezoelectric Actuators and Panel Interactions.....	5
2.3 Optimization.....	8
<b>Chapter 3: Methodology</b> .....	<b>12</b>
3.1 Rocha’s Model.....	14
3.2 Berry’s Model.....	20
3.3 Panel Excitations and Modified Berry’s Model .....	21
<b>Chapter 4: Experimental Setup</b> .....	<b>29</b>
4.1 NASA Validation Case.....	29
4.2 DLR Experimental Test Setup.....	33
4.3 Carleton University Experimental Test Setup .....	34

<b>Chapter 5: Results</b> .....	<b>38</b>
5.1 Panel Parameter Sensitivity Study and Panel Length Optimization.....	38
5.2 Analytical Model Validations for Different Excitations .....	48
5.2.1 Impact Hammer.....	48
5.2.2 TBL Excitation.....	53
5.2.3 Piezoelectric Patch Excitation.....	56
5.3 Optimal Piezoelectric Patch Positions to Reproduce TBL Excitation on the Panel .....	59
<b>Chapter 6: Conclusions and Future Work</b> .....	<b>64</b>
6.1 Panel Parameter Optimization .....	64
6.2 Experimental Setup .....	65
6.3 Analytical Model Validations for Different Excitations .....	65
6.4 Piezoelectric Patch Placement Optimization to Reproduce Acceleration PSD for a TBL Excitation.....	66
<b>References</b> .....	<b>67</b>
<b>Appendices</b> .....	<b>74</b>
Appendix A - Simply Supported Boundary Condition Test Setup.....	74

## List of Tables

<b>Table 1:</b> NASA Experimental Test Parameters [64].....	30
<b>Table 2:</b> Initial panel parameters for optimization.....	39
<b>Table 3:</b> Physical properties of the test panel. ....	49
<b>Table 4:</b> Flight condition parameters for TBL.....	54
<b>Table 5:</b> Panel modes required for Berry's and Rocha's models for different frequencies.....	55
<b>Table 6:</b> Piezoelectric patch parameters.....	57

## List of Figures

<b>Figure 1:</b> Flow progression over a surface from Laminar to Turbulent [2].....	2
<b>Figure 2:</b> Airflow over an airfoil depicting the transition point from laminar to turbulent flow [3].....	2
<b>Figure 3:</b> Aircraft fuselage construction depicting an aircraft panel as the area enclosed between the stringers and the formers [4].....	14
<b>Figure 4:</b> Sample definitions of optimizing problems as defined in graphical representation [51]. .....	10
<b>Figure 5:</b> Flow chart of research done with corresponding inputs at each stage. ....	13
<b>Figure 6:</b> Experimental test setup used by Heatwole [1,64]. ....	29
<b>Figure 7:</b> Predicted results as calculated by new Matlab code for the acceleration PSD given the NASA experimental test setup [64]. ....	31
<b>Figure 8:</b> Predicted results as calculated by Rocha for the acceleration PSD given the NASA experimental test setup (same results used to validate Rocha’s Model given a TBL excitation) [1,64]. ....	31
<b>Figure 9:</b> Front view of the DLR test setup. ....	33
<b>Figure 10:</b> Excitation and monitoring system of the DLR test setup, using a piezoelectric patch and an accelerometer.....	34
<b>Figure 11:</b> Front view of the constructed Carleton University test setup. ....	35
<b>Figure 12:</b> Rear view of the constructed Carleton University test setup. ....	35
<b>Figure 13:</b> Robin’s [47] summarized diagram of experimental setups that represent simply supported boundary conditions by: (a) Ochs [43] (b) Champoux [44] (c) Hoppmann [45] and Barnard [46] .....	36

<b>Figure 14:</b> A look at the 80% thickness cut in an aluminum panel to represent simply supported boundary conditions.....	37
<b>Figure 15:</b> Percent change in acceleration PSD versus percent change in panel parameter for octave 89.1-178 Hz with limited Y-axis extents.....	39
<b>Figure 16:</b> Percent change in acceleration PSD versus percent change in panel parameter for octave 178-355 Hz with limited Y-axis extents.....	40
<b>Figure 17:</b> Percent change in acceleration PSD versus percent change in panel parameter for octave 355-708 Hz with limited Y-axis extents.....	40
<b>Figure 18:</b> Percent change in acceleration PSD versus percent change in panel parameter for octave 708-1410 Hz with limited Y-axis extents.....	41
<b>Figure 19:</b> Optimal panel length at the center frequency of different octave bands that result in a local minimum average acceleration PSD compared to the calculated flexural wavelength, convective wavelength and acoustic wavelength [66].....	44
<b>Figure 20:</b> Optimal panel length at individual frequencies that result in a global minimum average acceleration PSD compared to the calculated flexural wavelength, convective wavelength and acoustic wavelength for two octave bands (up to 700 Hz).....	46
<b>Figure 21:</b> Optimal panel length at individual frequencies that result in a global minimum average acceleration PSD compared to the calculated flexural wavelength, convective wavelength and acoustic wavelength for four octave bands.....	47
<b>Figure 22:</b> Comparison of acceleration PSD results for a panel with simply supported boundary conditions at a point $x = 20.6$ cm and $y = 21.6$ cm, with a point force applied at $x = 7.7$ cm and $y = 3.8$ cm for three different models. ....	49

**Figure 23:** Comparison of acceleration PSD results for a panel with free boundary conditions at a point  $x = 20.6$  cm and  $y = 21.6$  cm with a point force applied at  $x = 7.7$  cm and  $y = 3.8$  cm for two different models. .... 51

**Figure 24:** Comparison of predicted (solid line) vs. experimental (dashed line) of acceleration PSD results for a panel with arbitrary boundary conditions at: (a) measured at (M):  $x = 5.4$  cm,  $y = 13.6$  cm and force applied at (F):  $x = 5.4$  cm and  $y = 13.6$  cm (b) M:  $x = 31.2$  cm,  $y = 32.1$  cm and F:  $x = 31.2$  cm and  $y = 32.1$  cm (c) M:  $x = 31.2$  cm,  $y = 32.1$  cm and F:  $x = 4.5$  cm and  $y = 3.9$  cm (d) M:  $x = 31.2$  cm,  $y = 32.1$  cm and F:  $x = 4.2$  cm and  $y = 19.8$  cm (e) M:  $x = 31.2$  cm,  $y = 32.1$  cm and F:  $x = 4.2$  cm and  $y = 32.2$  cm (f) M:  $x = 31.2$  cm,  $y = 32.1$  cm and F:  $x = 10.6$  cm and  $y = 26.0$  cm..... 52

**Figure 25:** Comparison of acceleration PSD results for a panel with simply supported boundary conditions at a point  $x=a/4$  and  $y = b/4$  with a TBL excitation applied..... 54

**Figure 26:** Comparison of acceleration PSD results for a panel with simply supported boundary conditions at a point  $x=a/4$  and  $y = b/4$ , with a TBL excitation applied. Each target frequency is calculated with the same constant number of panel modes  $m, n = 9,7$ . .... 55

**Figure 27:** Comparison of acceleration PSD results for a panel with simply supported boundary conditions at a point  $x=a/4$  and  $y = b/4$ , with a TBL excitation applied. Each target frequency is calculated with the same constant number of panel modes  $m, n = 14,11$ . .... 56

**Figure 28:** Comparison, using Berry’s model, of predicted (solid line) vs. experimental (dashed line) of acceleration PSD results for a panel with arbitrary boundary conditions: (a) measured at (M):  $x = 26.2$  cm,  $y = 8.6$  cm with a piezoelectric actuator excitation applied at (F):  $x = 12.3$  cm,  $y = 7.4$  cm (b) M:  $x = 31.4$  cm,  $y = 26.0$  cm and F:  $x = 12.3$  cm,  $y = 7.4$  cm (c) M:  $x = 31.4$  cm,

y = 26.0 cm and F: x = 15.5 cm, y = 26.0 cm (d) M: x = 25.5 cm, y = 13.4 cm and F: x = 15.5 cm, y = 26.0 cm ..... 58

**Figure 29:** Optimal single piezoelectric patch position and alternating voltage potential (X = 0.4470 m, Y = 0.1789 m,  $\Delta\varphi_{pz} = 3.4045$  V) to best reproduce the acceleration PSD of a panel caused by the TBL at constant cruise conditions..... 61

**Figure 30:** Optimal configuration of two piezoelectric patches positions and alternating voltage potentials (X1 = 0.4127 m, Y1 = 0.0211 m,  $\Delta\varphi_{1pz} = 6.1852$  V, X2 = 0.0804 m, Y2 = 0.0513 m,  $\Delta\varphi_{2pz} = 0.0301$  V) to best reproduce the acceleration PSD of a panel caused by the TBL at constant cruise conditions. .... 62

**Figure 31:** Optimal configuration of three piezoelectric patches positions and alternating voltage potentials (X1 = 0.3967 m, Y1 = 0.0224 m,  $\Delta\varphi_{1pz} = 7.0608$  V, X2 = 0.1964 m, Y2 = 0.0283 m,  $\Delta\varphi_{2pz} = 2.1062$  V, X3 = 0.0439 m, Y3 = 0.0208 m,  $\Delta\varphi_{3pz} = 0.0114$  V) to best reproduce the acceleration PSD of a panel caused by the TBL at constant cruise conditions. .... 63

## List of Appendices

Appendix A: Simply Supported Boundary Condition Test Setup.....	74
---	----

## List of Abbreviations

TBL	Turbulent Boundary Layer
PZT	Piezoelectric Transducer
RSP	Radiated Sound Power
PSD	Power Spectral Density
AC	Alternating Current
CNC	Computer Numerically Controlled
DLR	Deutsches Zentrum für Luft- und Raumfahrt
FEM	Finite Element Method

## Nomenclature

$a$	Panel length [m]
$b$	Panel width [m]
$C_f$	Friction coefficient
$D_p$	Panel bending stiffness [N m]
$D_{pp}$	Damping matrix (Rocha's Model)
$e_{31}^{pz}$	Effective piezoelectric transverse coefficient
$e_{32}^{pz}$	Effective piezoelectric transverse coefficient
$E_p$	Panel elasticity modulus [Pa]
$f_{mn}$	Force function matrix based on the excitation
$f(\omega)$	Frequency response of an input force from an impact hammer
$F_{m_x m_y}^{pz}$	Piezoelectric patch excitation PSD
$h_p$	Panel thickness [m]
$H(\omega)$	Frequency response matrix of a system
$\tilde{K}_{mnpq}$	Complex stiffness matrix (Berry's model)
$K_{pp}$	Stiffness matrix (Rocha's model)
$L_x^{pz}$	Length of the piezoelectric patch [m]
$L_y^{pz}$	Width of the piezoelectric patch [m]
$L_z^{pz}$	Thickness of the piezoelectric patch [m]
$m_x, m_y$	Plate mode
$M$	Total number of plate modes considered
$(M_{Max}, N_{Max})$	Number of panel modes required to satisfy the convergence test
$M_{mnpq}$	Mass matrix (Berry's Model)
$M_{pp}$	Mass matrix for a panel (Rocha's Model)
$N_{Ma}$	Mach number
$N_x$	Panel longitudinal tension [N m <sup>-1</sup> ]
$N_y$	Panel lateral tension [N m <sup>-1</sup> ]
$P_{tbl}(\omega)$	Pressure fluctuations due to the TBL
$q_{m_x m_y}(t)$	Function defining the variation in $w(x,y,t)$ with respect to time
$Re_x$	Reynolds number

$S(\zeta_x, \zeta_y, \omega)$	Corcos Model
$S_{aa}(\omega)$	Acceleration PSD
$S_e(\omega)$	Excitation PSD
$S_{ref}(\omega)$	Efimov's model of the TBL pressure spectrum
$S_{tbl}(\omega)$	TBL excitation PSD
$S_{vv}(\omega)$	Velocity PSD
$S_{ww}(\omega)$	Displacement PSD
Sh	Strouhal number
T	Temperature [K]
$T_w$	Temperature at the boundary wall [K]
$U_c$	Convection velocity [m/s]
$U_i$ or $U_\infty$	Freestream velocity [m/s]
$U_T$	Friction velocity [m/s]
$w(x,y,t)$	Displacement with respect to time at a single point [m]
$w(x,y, \omega)$	Displacement with respect to frequency at a single point [m]
x	Stream wise position [m]
$X(\omega)$	Frequency dependant excitation function
y	Span wise position [m]
$Y(\omega)$	Frequency dependant response of a system from $X(\omega)$
$\alpha_{m_x}(x)$	Spatial function in stream wise direction
$\beta_{m_y}(y)$	Spatial function in span wise direction
$\delta$	Boundary layer thickness [m]
$\delta^*$	Boundary layer displacement thickness [m]
$\Delta\phi^{pz}$	Voltage across the piezo electric patch [V]
$\rho_p$	Panel density [ $\text{kg m}^{-3}$ ]
$\lambda$	Wavelength of the plate bending wave [m]
$\nu$	Kinematic viscosity [ $\text{m}^2\text{s}^{-1}$ ]
$\nu_p$	Poisson ratio
$\nu_w$	Kinematic viscosity at the wall [ $\text{m}^2\text{s}^{-1}$ ]
$\omega$	Angular frequency [rad/s]
$\omega_{m_x m_y}^p$	Natural frequency corresponding to a panel mode [rad/s]
$\zeta_p$	Damping ratio
$\zeta_x$	Spatial separation in the stream wise direction
$\zeta_y$	Spatial separation in the span wise direction

# **Chapter 1: Introduction**

## **1.1 Objective**

This thesis develops a method to analytically optimize an aircraft's cabin panel parameters to best reduce the acceleration Power Spectral Density (PSD) of the panel caused by the Turbulent Boundary Layer (TBL), thereby reducing the Radiated Sound Power (RSP) into the cabin of the aircraft. In addition, a method to reproduce the acceleration power spectral density of an aircraft panel in constant cruise conditions, to reduce expensive flight and/or wind tunnel tests is presented, by optimally selecting the placement of a given number of piezoelectric actuators, excited with a white noise distribution of frequencies within the human hearing range (20 – 20000 Hz). The analytical results are compared against experimental results from a panel tested in a semi-anechoic chamber.

## **1.2 Motivation**

The noise and vibration in an aircraft cabin, during cruise conditions, is predominantly caused by the external TBL [1]. The TBL causes the fuselage panels on the aircraft to vibrate, which radiate sound energy in the form of noise in the cabin. Figure 1 and Figure 2 show the turbulent boundary layer and how the laminar flow, as it travels across a surface, gets tripped. This causes eddies, which produces a layer of fluctuating pressure (a turbulent layer) on top of the surface.

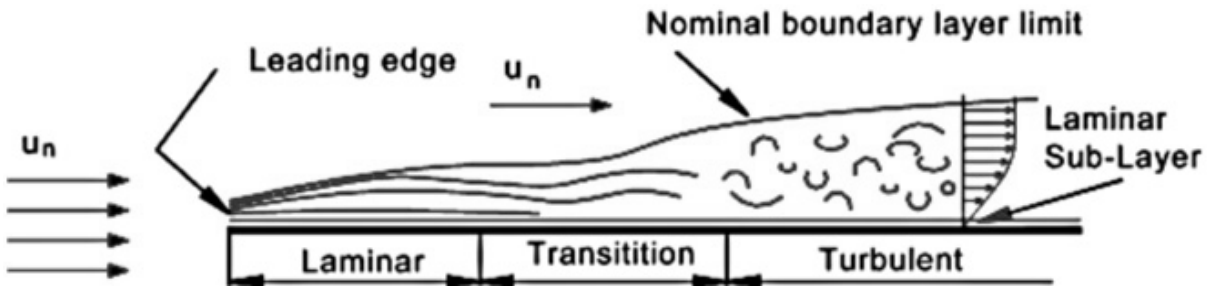


**Figure 1:** Flow progression over a surface from Laminar to Turbulent [2].

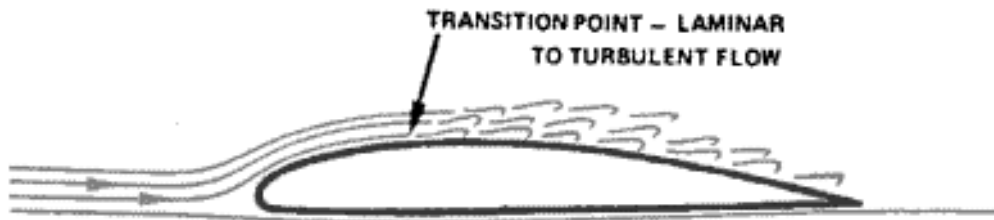


**Figure 2:** Airflow over an airfoil depicting the transition point from laminar to turbulent flow [3].

Airplane noise has been measured at an average of 80 to 85 decibels [5], with higher sound pressure levels during engine start and takeoff, and some researchers have noted an increased risk of hearing loss in cabin crew with exposures between 71 and 81 decibels [6]. Aircraft cabin noise has been shown to be related to hearing loss and the risk of cardiac disease for frequent fliers [7,8]. Therefore, by reducing the noise on the inside of the cabin of an aircraft flight attendants, pilots and passengers can have improved health, comfort and satisfaction. It is therefore beneficial to aircraft designers to be capable of optimally reducing the noise on the inside of the cabin with early design choices and through inexpensive and accurate testing methods.

The current methods for testing the amount of RSP and ways of reducing it are expensive. These types of tests are required to be performed in expensive flight testing or using wind tunnel testing. This thesis details the effects of the TBL on the aircraft panels by using piezoelectric actuators to vibrate the panel. This objective is accomplished by using modified analytical models that have been validated against experimental results.

The current work is applicable to reducing and reproducing the amount of noise in the cabin of an aircraft during cruise conditions from a vibrating panel excited by the TBL. It does not detail the effects, on the noise, of modifying an aircraft panel during takeoff and landing. It is also not able to accurately reproduce the noise due to turbulence during those stages of flight. The models only allow for the noise to be reproduced due to the vibration of the panel from the TBL. However, the other sources of noise that are present during cruise flight conditions (engine noise, passenger communications, etc.) are not taken into account in these models.

### **1.3 Contributions to State of the Art**

The author has made many contributions to the state of the art with their developed software. The following is a list of these contributions:

- (1) By creating a program that allows the user to generate an optimal panel for a given flight condition (e.g. cruise flight), it provides the aerospace industry another tool to improve passenger comfort when designing a new aircraft. Aircraft designers will be able to give bounds to each parameter that they can vary, which depend on the aircraft's structural fatigue requirements and weight restrictions and provide designers the best panel configuration, within those bounds, to reduce noise inside the

cabin. Currently, no such software exists that can optimize the panel parameters of an aircraft cabin panel to best reduce the noise from the TBL inside an aircraft.

- (2) The program created in the present study calculates the optimal position of piezoelectric actuators on a panel, to best replicate the acceleration PSD of an aircraft panel in constant cruise flight conditions, providing a method to reduce currently costly acoustic, flight and wind tunnel testing, by using a more inexpensive and simpler approach on the ground in an acoustically treated environment. This allows acoustic testing to be performed prior to the final aircraft being manufactured, which may result into changes to the design being made before it becomes too costly.
- (3) Current aircraft have minimal early design work in regards to reducing noise in the aircraft cabin. It is currently left to the end of the design stage whereby it is measured and improvements are implemented to best help whatever it has yielded. This software allows for the evaluation to happen early in the preliminary design phase, considering noise to be a design parameter right at the beginning of the design stage.
- (4) This work has resulted, so far, in one journal [9] and one conference [10] papers published, and one additional journal paper that has been submitted and is under review.

## **Chapter 2: Literature Review**

### **2.1 Acceleration Power Spectral Density and Radiated Sound Power**

Many researchers have studied the prediction of the response of a simple panel due to the TBL. Strawderman and Brand have some of the earliest simulated results for a turbulent flow excited panel vibration [11]. Others have modelled the response of the plate using wavenumber-frequency formulations, or have used finite element and boundary element methods, where the plate is excited by a number of distributed forces having proper spatial and temporal correlations [12–15].

One approach to calculate the RSP of vibrating structures is to use a modal analysis, as done by Roy and Lapi [16]. This approach is necessary when analyzing obscure shapes, but requires great computational power and time, making it difficult to iterate the calculations for optimization routines. Therefore, when looking at simple shapes, like that of a flat panel, analytical computational methods become a better choice. The analytical expressions for RSP can be derived for a given aircraft panel, in terms of the displacement PSD [1,17,18]. The acceleration PSD is calculated from the displacement PSD, which is proportional to the RSP [18]. The analytical models developed, by Rocha, were modified to account for other panel and enclosure combinations [19,20]. Berry showed that the same type of analytical analysis was possible for panels with arbitrary boundary conditions [21]. Charrette and Berry also showed it was possible to include the effects of piezoelectric patches into this model [22].

### **2.2 Piezoelectric Actuators and Panel Interactions**

Piezoelectricity was discovered in 1889 by Jacques and Pierre Curie [23]. They discovered that certain materials, such as quartz, when put under a compressive or tensile forces

in the direction of the axis of symmetry, produce electrical polarization of the material. It was later discovered by Lippman that the opposite was also true, that when certain materials were exposed to a voltage potential the material would deform in the direction of the applied voltage [24]. A piezoelectric actuator is a device that makes use of this principle. An Alternating Current (AC) is applied to the ends of the piezoelectric material which causes it to expand and contract with the frequency of the AC. These types of actuators have many applications from ultrasound transmitters for medical and range-finding uses, microrobotic applications, hard disk drive head positioning, immunosensors and many more [25–31].

Over the past 20 years, there have been many applications of piezoelectric actuators to actively control vibration of materials [32–34]. Some of these studies have even focused on actively reducing the vibration of aircraft panels to reduce the amount of noise into the cabin. However, most of these techniques use feedback loops from information provided by sensors on the panel to adjust the actuation until the vibration has been minimized. These techniques often lack direct models showing how a single actuator affects the vibration at a different point on the panel. This study will confirm an analytical model by which the vibration at a point on a panel can be predicted by the panel parameters, and the location and properties of a given piezoelectric actuator bonded to the panel. A white noise distribution of frequency signals, in the human hearing range, is fed to the actuators to reduce the complexity and cost of the system, while still maintaining the same level of noise reduction. The objective of this study is to optimize the replication of the acceleration PSD, of an aircraft panel from the TBL with piezoelectric actuators that are given the same white noise distribution of frequencies, and by selecting the optimal positions of the actuators of the panel.

The current methods of testing the amount of RSP and testing possible solutions for reduction, are expensive. These types of tests are required to be performed in-flight or through expensive wind tunnel testing. By using piezoelectric actuators to vibrate the panel, the effects of the TBL on the panel will be recreated without the need of those expensive tests. Other studies have attempted to reproduce the TBL excitation using loudspeakers [35–41]. It was found that at low frequencies, accurate reproduction can be obtained, however, the higher the frequency range, the more loudspeakers are required and the more complex the control signals become. It has been predicted that using piezoelectric patches to excite the panel may require less actuators than loudspeakers to obtain the same quality of reproduction at low frequencies, and it might allow the response to be reproduced at higher frequency ranges, because it removes the air gap in between the excitation device and the panel [42]. Piezoelectric patches also come in varying sizes, allowing more to be bonded to the panel than the amount of loudspeakers that can be arranged in front of the panel.

There have been many experimental setups used to try to replicate an aircraft panel. Some have attempted to reproduce a panel with simply supported boundary conditions, which allows the equations for the acceleration PSD response to be simplified [43–47]. However, these experimental setups are either very difficult to manufacture or are structurally weak for a thin aircraft panel. Additionally, true aircraft panels, which are assumed to be simply supported for most of the tests outlined in this paper, are not actually simply supported as they often have boundary conditions in between simply supported and clamped conditions. Therefore, the experimental setup used to validate Berry's model for arbitrary boundary conditions is the one used at Deutsches Zentrum für Luft- und Raumfahrt (DLR) [41,48].

### 2.3 Optimization

Optimization means finding the best solution among many feasible solutions that are available. Feasible solutions are those that satisfy all the constraints in the optimization problem [49]. Beightler described optimization as a three step decision making process: obtain knowledge of the system (model the system), find a measure of the systems effectiveness (objective function), and the theory of optimization [50]. Fundamentally, he says one must first understand the systems they want to optimize by understanding the mathematical model that relates inputs to outputs. Then a way to evaluate the system (cost, efficiency, weight, etc.) is required, which is called the objective function, and finally, one must optimize the systems inputs (the design variables) to result in a minimum or maximum for the given objective equation.

An optimization problem can be defined mathematically as [49,51]:

Minimize:

$$f(x) \tag{1}$$

Subject to:

$$g_i(x) \leq 0 \quad i = 1,2, \dots, m < n \tag{2}$$

$$h_j(x) = 0 \quad j = 1,2, \dots, r < n \tag{3}$$

$$x_l \leq x \leq x_u \tag{4}$$

Where  $x$  is a vector of  $n$  design variables given by:

$$x = \begin{bmatrix} x_1 \\ x_2 \\ \vdots \\ x_n \end{bmatrix} \quad (5)$$

In this work the function  $f$ ,  $g_i$  and  $h_j$  are all assumed to be differentiable. The design variables are bounded by the lower and upper limits,  $x_l$  and  $x_u$ , respectively. The constraints in  $g_i$  are inequality constraints compared to the equality constraints in  $h_j$ . The constraints are functions of the design variables and there must be fewer constraints than the number of design variables. If the design variables, within their bounds, can be proven to satisfy all of the constraints, then there exists a feasible region. This feasible region can be solved through a number of methods to determine the optimal design variables which minimize the objective function. Figure 3 shows how an optimization problem can be represented in graphical form, to better show the feasible region and the objective function. It shows a feasible region (an area) that exists in between the defined constraints (Left). The optimal design variables are those which minimize the objective function while maintaining design variables in the feasible region (Right).

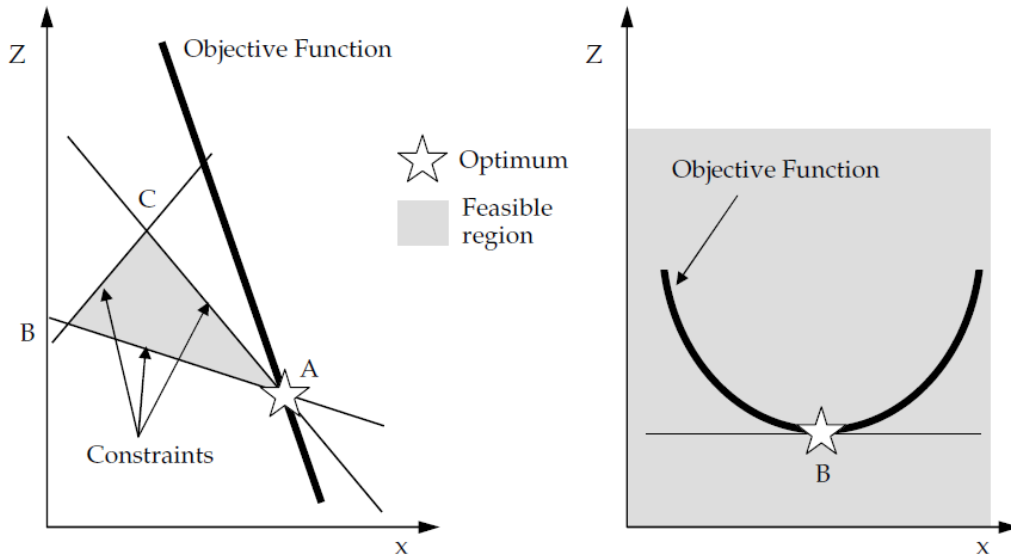


**Figure 3:** Sample definitions of optimizing problems as defined in graphical representation [51].

After the optimization problem can be defined, there are many options when it comes to solving the problem. Optimization algorithms are usually iterative, beginning with an initial guess and then continuing to make improved estimates until the program terminates, ideally when it has converged at a minimum. The process by which the algorithm selects the next estimate is the defining feature of the algorithm. Good algorithms should be robust, efficient and accurate [52].

There are many free software codes available that can be used for optimization. The optimizing code used throughout this study is an add-on to Matlab. It uses an interior point algorithm for a nonlinear equation. The specific optimization settings used throughout this thesis are the default Matlab “fmincon” options [53]. An interior point algorithm is an approach to constrained minimization that solves a sequence of approximate minimization problems [54]. This is different from the simplex method which moves its iterations along the boundary of the feasible region from one extreme point to another [55]. In the past 30 years there has been

significant advancement in interior point methods after the work of Karmarkar in 1984 [56]. Many books have been written explaining the basics of the method and the applications it has for both linear and nonlinear functions [55,57,58]. This type of algorithm has been used to optimize electrical power systems, shakedown analysis of pavements and power flow unsolvability [59–61]. The algorithm can be used for many applications and therefore it was selected to obtain initial optimized design variables.

### Chapter 3: Methodology

Two main models, Rocha's model [1,8–11] and Berry's model [12,27], have been used in this study, and further modified to account for different excitations. Rocha's model is an analytical approach for a panel with simply supported boundary conditions and uses trigonometric spatial functions [1,8–11]. Berry's model is developed for a panel with arbitrary boundary conditions and uses polynomial spatial functions [12,27]. The following sections briefly describes each model and different excitations used and Figure 4 shows a visual representation of the progression of the research and which models, excitations, experimental setups and boundary conditions are used as inputs for each step in the research.

All of the models and excitations have been modified to be in terms of the PSD domain. The PSD domain is used in this work because the TBL excitation is only able to be modelled in terms of a statistical representation. It is only possible to determine the probability of a given pressure on the panel at any point in time but it is not possible to predict the exact pressure at any given time, which means using the frequency domain would not be possible. The PSD of a given frequency response can be defined as follows:

$$S(\omega) = \frac{1}{2\pi} \int_{-\infty}^{\infty} R(\tau) e^{-i\omega\tau} d\tau \quad (6)$$

Where  $R(\tau)$  is the autocorrelation function of a random process in the time domain and  $F(t)$  is that random process as a function of time, defined as follows:

$$R(\tau) = \lim_{t_o \rightarrow \infty} \frac{1}{2t_o} \int_{-t_o}^{t_o} F(t) F(t + \tau) dt \quad (7)$$

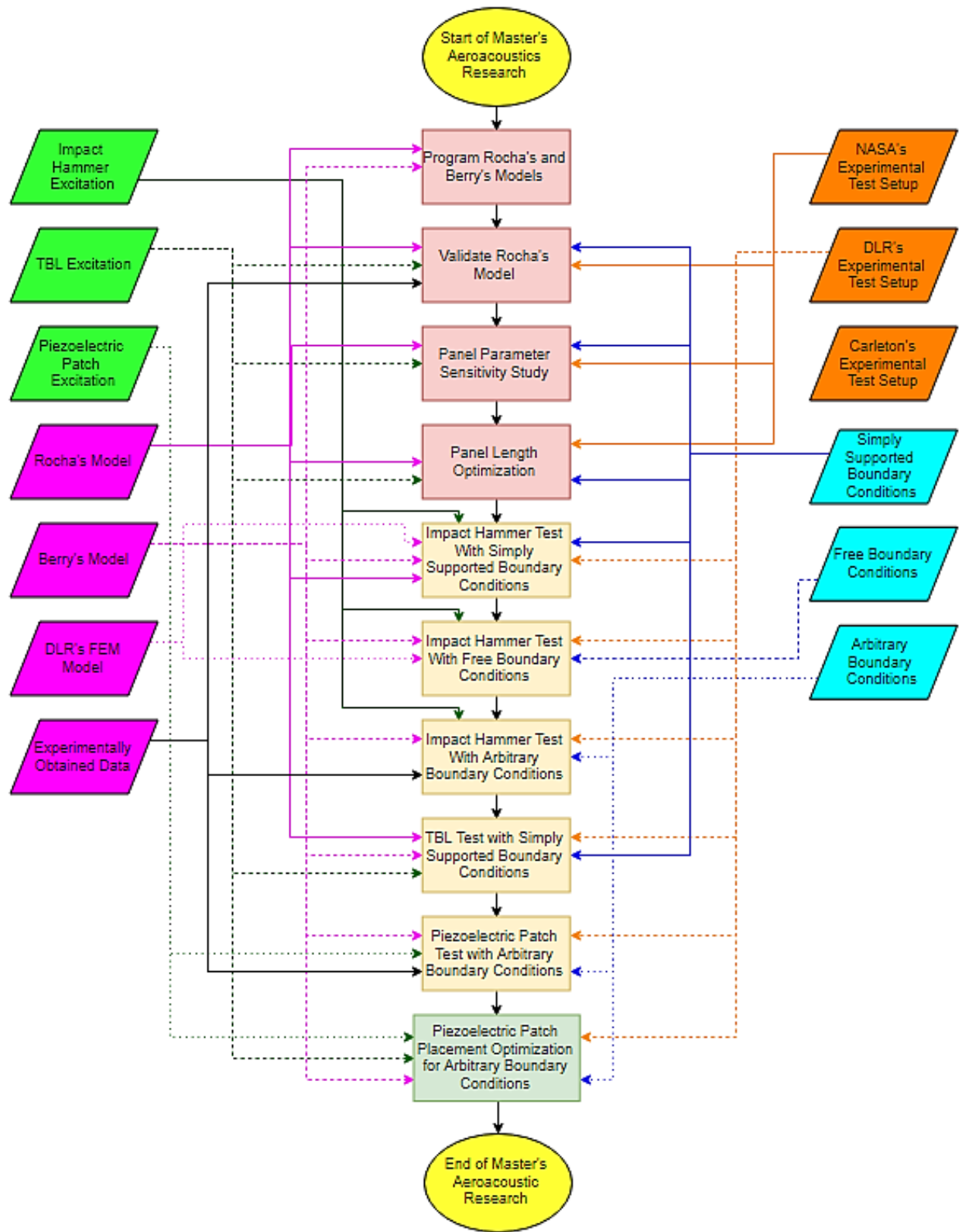
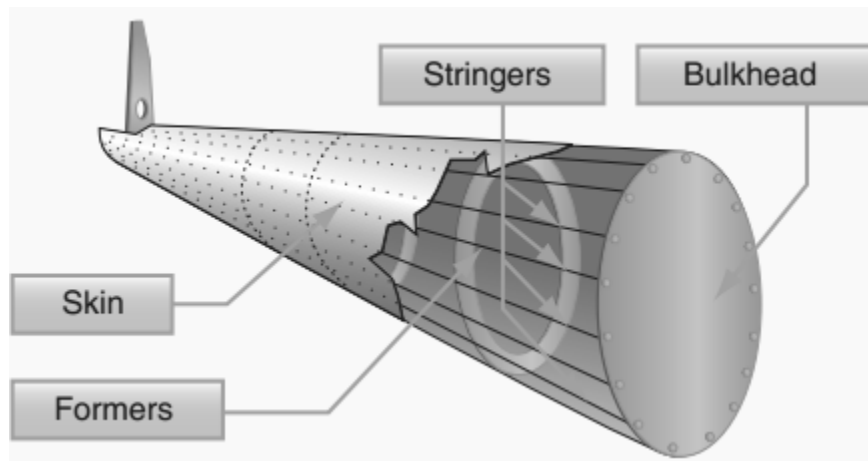


Figure 4: Flow chart of research done with corresponding inputs at each stage.

### 3.1 Rocha's Model

In this model, the panel is assumed to be flat and simply supported on all four sides. An aircraft panel may be defined as the enclosed area on a sheet of material, between adjacent stringers and formers. The connections of material to stringers and formers cause that section of material to act approximately as a single, simply supported panel. This can be depicted in Figure 5.



**Figure 5:** Aircraft fuselage construction depicting an aircraft panel as the area enclosed between the stringers and the formers [4].

The vibration of a single panel, in terms of displacement, can be defined as [1]:

$$w(x, y, t) = \sum_{m_x=1}^{M_x} \sum_{m_y=1}^{M_y} \alpha_{m_x}(x) \beta_{m_y}(y) q_{m_x m_y}(t) \quad (8)$$

In which  $q_{m_x m_y}(t)$  defines the variation in displacement with respect to time and  $\alpha_{m_x}$  and  $\beta_{m_y}(y)$  are spatial functions that define the variation in vibration and can be defined as follows, for a simply supported plate [1]:

$$\alpha_{m_x}(x) = \sqrt{\frac{2}{a}} \sin\left(\frac{m_x \pi x}{a}\right) \quad (9)$$

$$\beta_{m_y}(y) = \sqrt{\frac{2}{b}} \sin\left(\frac{m_y \pi y}{b}\right) \quad (10)$$

The first step in calculating the acceleration PSD is to determine the panel modes  $(m_x, m_y)$  and the natural frequency  $(\omega_{m_x m_y}^P)$  that corresponds with each mode, as follows [19]:

$$\omega_{m_x m_y}^P = \sqrt{\frac{1}{\rho_p h_p} \left\{ D_p \left[ \left(\frac{m_x \pi}{a}\right)^2 + \left(\frac{m_y \pi}{b}\right)^2 \right]^2 + N_x \left(\frac{m_x \pi}{a}\right)^2 + N_y \left(\frac{m_y \pi}{b}\right)^2 \right\}} \quad (11)$$

where:

$$D_p = \frac{E_p h_p^3}{12(1 - \nu_p^2)} \quad (12)$$

This equation can be simplified when assuming the panel is not under tension in either direction. The simplified equation can be seen below [19]:

$$\omega_{m_x m_y}^P = \sqrt{\frac{D_p}{\rho_p h_p} \left[ \left( \frac{m_x \pi}{a} \right)^2 + \left( \frac{m_y \pi}{b} \right)^2 \right]} \quad (13)$$

In order to determine how many modes are needed at a specific individual frequency, a convergence test must be completed. Convergence is reached when the distance between two nodes of the structural mode shape is less than, or equal to, one half-wavelength,  $\lambda/2$ , of the bending wave on the plate at the analysis frequency [19]. These values must be rounded to the next highest whole number, to coincide with a plate modal number, as shown below [19]:

$$M_{Max} = 2a/\lambda \quad (14)$$

$$N_{Max} = 2b/\lambda \quad (15)$$

$$\lambda = 2\pi \left( \frac{D_p h_p}{\rho_p} \right)^{0.25} (\omega)^{-0.5} \quad (16)$$

The convergence test determines the point at which additional panel modes are assumed to not change the overall shape of the final plot, but instead, appear to make the plot slightly noisier. By running a convergence test at every target frequency, it allows the program to limit the number of panel modes used for lower target frequencies, increasing the computational time to run the program.

The panel was originally modelled by Rocha to assume that it enclosed a cavity. The plate governing equation, for a given applied external pressure, is defined as [1]:

$$D_p \nabla^4 w + \rho_p h_p \ddot{w} + \zeta_p \dot{w} = p_{ext}(x, y, t) \quad (17)$$

With the assumption that there is also a cavity, an additional governing equation is defined. Rocha's research is able to reduce a coupled system of governing equations into the following matrix form [1]:

$$\begin{bmatrix} M_{pp} & 0 \\ M_{cp} & M_{cc} \end{bmatrix} \begin{Bmatrix} \ddot{q}(t) \\ \ddot{r}(t) \end{Bmatrix} + \begin{bmatrix} D_{pp} & 0 \\ 0 & D_{cc} \end{bmatrix} \begin{Bmatrix} \dot{q}(t) \\ \dot{r}(t) \end{Bmatrix} + \begin{bmatrix} K_{pp} & K_{pc} \\ 0 & K_{cc} \end{bmatrix} \begin{Bmatrix} q(t) \\ r(t) \end{Bmatrix} = \begin{Bmatrix} P_{tbl}(\omega) \\ 0 \end{Bmatrix} \quad (18)$$

This equation can be written as follows in terms of the system input ( $X(\omega)$ ), output ( $Y(\omega)$ ) and its frequency response ( $H(\omega)$ ) [1]:

$$Y(\omega) = H(\omega)X(\omega) \quad (19)$$

$$Y(\omega) = \begin{Bmatrix} W(\omega) \\ P(\omega) \end{Bmatrix} \quad (20)$$

$$X(\omega) = \begin{Bmatrix} P_{tbl}(\omega) \\ 0 \end{Bmatrix} \quad (21)$$

$$H(\omega) = \begin{bmatrix} -\omega^2 M_{pp} + i\omega D_{pp} + K_{pp} & K_{pc} \\ -\omega^2 M_{cp} & -\omega^2 M_{cc} + i\omega D_{cc} + K_{cc} \end{bmatrix}^{-1} \quad (22)$$

This matrix form assumes the panel is simply supported, and encloses a cavity (like the panels surrounding the enclosed cabin of the aircraft). The subscripts cc and cp represent the

physical properties of the cavity and how it interacts with the panel. In this study, only the panel is of interest and it is assumed there is no enclosed cavity, and therefore, these terms can be removed from the equation which reduces to:

$$H_w(\omega) = H(\omega) = [-\omega^2 M_{pp} + i\omega D_{pp} + K_{pp}]^{-1} \quad (23)$$

where [1]:

$$M_{pp} = \text{diag}[\rho_p h_p] \quad (24)$$

$$D_{pp} = \text{diag}[2\rho_p h_p \omega_m \zeta_p] \quad (25)$$

$$K_{pp} = \text{diag}[\rho_p h_p \omega_m^2] \quad (26)$$

Each of these matrices are of size MxM. With this information, the displacement PSD matrix ( $S_{ww}(\omega)$ ) can be defined as follows [1]:

$$S_{ww}(\omega) = H_w^*(\omega) S_e(\omega) H_w^T(\omega) \quad (27)$$

In this equation,  $S_e(\omega)$  is a generalized PSD matrix of the different excitations. The \* operator indicates the Hermitian conjugate of the matrix and the T operator is the transpose of the matrix. With this displacement PSD matrix, the displacement PSD at a single point can be calculated for a given frequency as follows [1]:

$$\begin{aligned}
& S_{WW}(x_1, y_1, x_2, y_2, \omega) \\
&= \sum_{m_{x_1}, m_{x_2}=1}^{M_x^2} \sum_{m_{y_1}, m_{y_2}=1}^{M_y^2} \alpha_{m_{x_1}}(x_1) \alpha_{m_{x_2}}(x_2) \beta_{m_{y_1}}(y_1) \beta_{m_{y_2}}(y_2) S_{ww}(\omega)_{m_1, m_2} \quad (28)
\end{aligned}$$

When  $x_1 = x_2$  and  $y_1 = y_2$  this calculates the autocorrelation at a single point and if these are not equal than it calculates the cross spectrum correlation between two different points. For the TBL excitation the autocorrelation is used and for the point force and the piezoelectric patch excitations the cross spectrum correlation is used. The equations required to calculate the velocity,  $S_{VV}$ , and the acceleration PSD,  $S_{AA}$ , at a single point on the panel are as follows [18]:

$$S_{VV} = \omega^2 S_{WW} \quad (29)$$

$$S_{AA} = \omega^4 S_{WW} \quad (30)$$

These equations are both proportional to frequency, which means that any conclusion made from graphs calculated from one equation, will have the same trend, but different magnitudes, as the other.

To show that calculating either  $S_{WW}$ ,  $S_{VV}$ , or  $S_{AA}$  will give direct correlations to their effects on the RSP of a panel, the basic equations required to calculate RSP have been provided [17]:

$$RSP(x_1, y_1, x_2, y_2, \omega) \quad (31)$$

$$= \sum_{m_{x_1}, m_{x_2}=1}^{M_x^2} \sum_{m_{y_1}, m_{y_2}=1}^{M_y^2} \alpha_{m_{x_1}}(x_1) \alpha_{m_{x_2}}(x_2) \beta_{m_{y_1}}(y_1) \beta_{m_{y_2}}(y_2) \prod(\omega)_{m_1, m_2}$$

$$\prod(\omega) = S_{VV} M(\omega) \quad (32)$$

These equations show that the RSP is proportional to  $S_{VV}$ , so any conclusions made from the sensitivity study on  $S_{AA}$ , will be proportional to the RSP. This allows for meaningful conclusions to be made about RSP without having to run a more time intensive program.  $M(\omega)$  is the radiation matrix previously defined by Rocha [17].

### 3.2 Berry's Model

The vibration of a single panel can still be defined as in equation (8), with the spatial functions defined as polynomial functions as follows [21]:

$$\alpha_{m_x}(x) = \frac{2}{a} x^{m_x} \quad (33)$$

$$\beta_{m_y}(y) = \frac{2}{b} y^{m_y} \quad (34)$$

A difference between the two methods is that Berry's model treats the panel mode indices as if they start at 0 instead of starting at 1. Similarly to equation (23), Berry defines the same equation as follows [21]:

$$(-\omega^2 M_{mnpq} + \tilde{K}_{mnpq})\{a_{mn}\} = \{f_{mn}\} \quad (35)$$

where:

$$mnpq = m_{x_1} m_{y_1} m_{x_2} m_{y_2} \quad (36)$$

$$a_{mn} = q_{m_x m_y} \quad (37)$$

$a_{mn}$  is solved for in equation (35) and is used to calculate the displacement PSD of the panel as follows:

$$w(x, y, \omega) = \sum_{m=1}^{M_x} \sum_{n=1}^{M_y} \alpha_m(x) \beta_n(y) a_{mn} \quad (38)$$

$$S_{ww}(\omega) = w(x, y, \omega) w(x, y, \omega)^* \quad (39)$$

### 3.3 Panel Excitations and Modified Berry's Model

For both of the models used, it is important to determine the correct way to represent the excitation. Rocha's model uses the excitation in its PSD form, whereas Berry's Model treats the excitation as a force spectrum. An impulse force can be represented as follows:

$$S_e(\omega) = f_{mn}(\omega) f_{mn}(\omega)^* \quad (40)$$

$$f_{mn}(\omega) = \alpha_m(x) \beta_n(y) f(\omega) \quad (41)$$

Here,  $f(\omega)$  is the frequency response of the force input as measured by the impact hammer. The spatial functions and mode numbering conventions change between the two models. However, using an impact force is the simplest excitation for both models.

The excitation from a TBL on the plate has previously been defined for Rocha's model. This work investigates the use of Rocha's model, for the TBL excitation, but uses polynomial spatial functions [1]. An analytical equation has been defined for use with Berry's model of a TBL excitation with polynomial spatial functions. Rocha defines the same process to determine an analytical equation for the TBL excitation PSD but for sinusoidal spatial functions. The following is the result of the same derivation, using polynomial spatial functions: the derivation starts with the Corcos model, which considers the cross power spectral density of the stationary and homogeneous turbulent boundary layer wall pressure field in a separable form in the streamwise, x-direction, and spanwise, y-direction, as follows [62,63]:

$$S(\zeta_x, \zeta_y, \omega) = S_{ref}(\omega) e^{-\frac{\alpha_x \omega |\zeta_x|}{U_c}} e^{-\frac{\alpha_y \omega |\zeta_y|}{U_c}} e^{-i \frac{\omega \zeta_x}{U_c}} \quad (42)$$

Therefore the power spectrum from a TBL is defined as:

$$S_{tbl}(\omega) = \int_{y_0}^{y_1} \int_{x_0}^{x_1} \phi_m(x) \phi_n(y) \phi_p(x') \phi_q(y') S(\zeta_x, \zeta_y, \omega) dx dy dx' dy' \quad (43)$$

Where the spatial separations in the streamwise and spanwise directions are  $\zeta_x = x - x'$  and  $\zeta_y = y - y'$ . The polynomial spatial functions can be defined as:

$$\Phi_m(x) = \alpha^m \quad (44)$$

$$\varphi_n(y) = \beta^n \quad (45)$$

where  $-1 \leq \alpha, \beta \leq 1$  and:

$$\alpha = \frac{2x}{a} \quad (46)$$

$$\beta = \frac{2y}{b} \quad (47)$$

After substituting equation (42) and the polynomial spatial functions into (43) the following results:

$$\frac{S_{tbl}(\omega)}{S_{ref}(\omega)} = \iint_{x_0}^{x_1} \alpha^m \alpha'^p e^{-\frac{\alpha_x \omega |\zeta_x|}{U_c}} e^{-i \frac{\omega \zeta_x}{U_c}} dx dx' \iint_{y_0}^{y_1} \beta^n \beta'^q e^{-\frac{\alpha_y \omega |\zeta_y|}{U_c}} dy dy' \quad (48)$$

let:

$$x_0 = \frac{a}{2} \alpha_0; \quad x_1 = \frac{a}{2} \alpha_1; \quad y_0 = \frac{b}{2} \beta_0; \quad y_1 = \frac{b}{2} \beta_1 \quad (49)$$

and  $-1 \leq \alpha_0, \alpha_1, \beta_0, \beta_1 \leq 1$ , therefore:

$$\frac{S_{tbl}(\omega)}{S_{ref}(\omega)} = \frac{a^2 b^2}{16} \iint_{\alpha_0}^{\alpha_1} \alpha^m \alpha'^p e^{-\frac{\alpha_x \omega a}{2U_c} |\alpha - \alpha'|} e^{-i \frac{\omega a}{2U_c} (\alpha - \alpha')} d\alpha d\alpha' \iint_{\beta_0}^{\beta_1} \beta^n \beta'^q e^{-\frac{\alpha_y \omega b}{2U_c} |\beta - \beta'|} d\beta d\beta' \quad (50)$$

This can be simplified to:

$$S_{tbl}(\omega) = S_{ref}(\omega) \frac{a^2 b^2}{16} S_\alpha S_\beta \quad (51)$$

let:

$$\mu = \frac{\alpha_x \omega a}{2U_c}; \quad \kappa = \frac{\omega a}{2U_c}; \quad \rho = \frac{\alpha_y \omega b}{2U_c} \quad (52)$$

Therefore:

$$\begin{aligned} S_\alpha &= \int_{\alpha_0}^{\alpha_1} \alpha^m e^{-(\mu+i\kappa)\alpha} \int_{\alpha_0}^{\alpha} \alpha'^p e^{(\mu+i\kappa)\alpha'} d\alpha' d\alpha + \int_{\alpha_0}^{\alpha_1} \alpha^m e^{(\mu-i\kappa)\alpha} \int_{\alpha}^{\alpha_1} \alpha'^p e^{-(\mu-i\kappa)\alpha'} d\alpha' d\alpha \\ &= S_L + S_U \end{aligned} \quad (53)$$

With a change of variables:

$$S_\beta \hat{=} S_\alpha \quad (54)$$

This occurs when  $\alpha_0 \rightarrow \beta_0$ ,  $\alpha_1 \rightarrow \beta_1$ ,  $\mu \rightarrow \rho$ ,  $\kappa \rightarrow 0$ ,  $\alpha \rightarrow \beta$  and  $\alpha' \rightarrow \beta'$ . Further simplification of these equations by setting  $z = \mu + i\kappa$  leads to:

$$S_L = \int_{\alpha_0}^{\alpha_1} \alpha^m e^{-z\alpha} \int_{\alpha_0}^{\alpha} \alpha'^p e^{z\alpha'} d\alpha' d\alpha \quad (55)$$

$$S_U = \int_{\alpha_0}^{\alpha_1} \alpha^m e^{\bar{z}\alpha} \int_{\alpha}^{\alpha_1} \alpha'^p e^{-\bar{z}\alpha'} d\alpha' d\alpha \quad (56)$$

$$S_U = \int_{\alpha_0}^{\alpha_1} \alpha'^p e^{-\bar{z}\alpha'} \int_{\alpha_0}^{\alpha} \alpha^m e^{\bar{z}\alpha} d\alpha d\alpha' \quad (57)$$

With a change of variables:  $m \rightarrow p$  and  $z \rightarrow \bar{z}$  then  $S_U \cong S_L$ . These equations can then be integrated to result in an analytical expression where  $S_L = f_{m,p}$  as shown below:

$$f_{m,p} = \frac{1}{z} \left[ m f_{m-1,p} - \alpha_1^m e^{-z\alpha_1} g_p + \frac{\alpha_1^{m+p+1} - \alpha_0^{m+p+1}}{m+p+1} \right] \quad (58)$$

$$g_p = \frac{1}{z} [\alpha_1^p e^{z\alpha_1} - \alpha_0^p e^{z\alpha_0} - p g_{p-1}] \quad (59)$$

Where:  $m, p \geq 0$  and  $f_{-1,p} = 0$  and  $g_{-1} = 0$

Therefore an analytical expression has been determined for  $S_{tbl}(\omega)$  with polynomial spatial functions.

The piezoelectric actuator excitation has previously been defined for Berry's Model by Charette and Berry [22]:

$$\begin{aligned}
F_{m_x m_y}^{pz} &= -\Delta\varphi^{pz}(h_p + L_z^{pz}) \\
& * \left\{ \frac{b e_{31}^{pz} m_x}{a(m_y + 1)} \left[ \left( \frac{2x^{pz} + L_x^{pz}}{a} \right)^{m_x - 1} - \left( \frac{2x^{pz} - L_x^{pz}}{a} \right)^{m_x - 1} \right] \right. \\
& * \left[ \left( \frac{2y^{pz} + L_y^{pz}}{b} \right)^{m_y + 1} - \left( \frac{2y^{pz} - L_y^{pz}}{b} \right)^{m_y + 1} \right] \\
& + \frac{a e_{32}^{pz} m_y}{b(m_x + 1)} \left[ \left( \frac{2x^{pz} + L_x^{pz}}{a} \right)^{m_x + 1} - \left( \frac{2x^{pz} - L_x^{pz}}{a} \right)^{m_x + 1} \right] \\
& * \left. \left[ \left( \frac{2y^{pz} + L_y^{pz}}{b} \right)^{m_y - 1} - \left( \frac{2y^{pz} - L_y^{pz}}{b} \right)^{m_y - 1} \right] \right\} \tag{60}
\end{aligned}$$

$(x^{pz}, y^{pz})$  is the distance from the center of the panel to the center of the plate in the length and width directions. They can be calculated as follows for the coordinate system defined below:

$$x^{pz} = \left| \frac{a}{2} - x_1 \right| \tag{61}$$

$$y^{pz} = \left| \frac{b}{2} - y_1 \right| \tag{62}$$

This treats the force from the piezoelectric patch as a point force located at its center. Charette and Berry show how to incorporate the effects of the piezoelectric patch to the mass and stiffness matrices of the panel [22]. These values often have very little effect on large panels due to the relative size of a single patch. However, it is important to include the patches impact in the model because the authors aim to modify the model to include multiple patches at different locations, which will have a more significant impact on the panels' mass and stiffness matrices,

as shown below. One major deviation in this work from Charette's paper [22], is that instead of using piezoelectric patches on both sides of the panel, there is only one patch on one side. Therefore the equations (60), (63), and (64), as defined here, are all divided by two:

$$\begin{aligned}
 M_{m_{x_1} m_{y_1} m_{x_2} m_{y_2}}^{pz} & \tag{63} \\
 &= \frac{\rho^{pz} L_z^{pz} L_x^{pl} L_y^{pl}}{2(m_{x_1} + m_{x_2} + 1)(m_{y_1} + m_{y_2} + 1)} \\
 & * \left[ \left( \frac{2x^{pz} + L_x^{pz}}{L_x^{pl}} \right)^{m_{x_1} + m_{x_2} + 1} - \left( \frac{2x^{pz} - L_x^{pz}}{L_x^{pl}} \right)^{m_{x_1} + m_{x_2} + 1} \right] \\
 & * \left[ \left( \frac{2y^{pz} + L_y^{pz}}{L_y^{pl}} \right)^{m_{y_1} + m_{y_2} + 1} - \left( \frac{2y^{pz} - L_y^{pz}}{L_y^{pl}} \right)^{m_{y_1} + m_{y_2} + 1} \right]
 \end{aligned}$$

$K_{m_{x_1} m_{y_1} m_{x_2} m_{y_2}}^{pz}$ 

(64)

$$\begin{aligned}
&= 2L_z^{pz} \left( \frac{(L_z^{pz})^2}{3} + [L_z^{pl} + L_z^{pz}]^2 \right) \\
&\quad * \left\{ \frac{Y_1^{pz} L_y^{pl} m_{x_1} (m_{x_1} - 1) m_{x_2} (m_{x_2} - 1)}{(L_x^{pl})^3 (m_{x_1} + m_{x_2} - 3) (m_{y_1} + m_{y_2} + 1)} \right. \\
&\quad * \left[ \left( \frac{2x^{pz} + L_x^{pz}}{L_x^{pl}} \right)^{m_{x_1} + m_{x_2} - 3} - \left( \frac{2x^{pz} - L_x^{pz}}{L_x^{pl}} \right)^{m_{x_1} + m_{x_2} - 3} \right] \\
&\quad * \left[ \left( \frac{2y^{pz} + L_y^{pz}}{L_y^{pl}} \right)^{m_{y_1} + m_{y_2} + 1} - \left( \frac{2y^{pz} - L_y^{pz}}{L_y^{pl}} \right)^{m_{y_1} + m_{y_2} + 1} \right] \\
&\quad + \frac{Y_1^{pz} L_x^{pl} m_{y_1} (m_{y_1} - 1) m_{y_2} (m_{y_2} - 1)}{(L_y^{pl})^3 (m_{y_1} + m_{y_2} - 3) (m_{x_1} + m_{x_2} + 1)} \\
&\quad * \left[ \left( \frac{2x^{pz} + L_x^{pz}}{L_x^{pl}} \right)^{m_{x_1} + m_{x_2} + 1} - \left( \frac{2x^{pz} - L_x^{pz}}{L_x^{pl}} \right)^{m_{x_1} + m_{x_2} + 1} \right] \\
&\quad * \left[ \left( \frac{2y^{pz} + L_y^{pz}}{L_y^{pl}} \right)^{m_{y_1} + m_{y_2} - 3} - \left( \frac{2y^{pz} - L_y^{pz}}{L_y^{pl}} \right)^{m_{y_1} + m_{y_2} - 3} \right] \\
&\quad + \frac{4Y_{66}^{pz} m_{x_1} m_{y_1} m_{x_2} m_{y_2} + Y_6^{pz} \left[ \begin{array}{l} m_{x_1} (m_{x_1} - 1) m_{y_2} (m_{y_2} - 1) \\ + m_{y_1} (m_{y_1} - 1) m_{x_2} (m_{x_2} - 1) \end{array} \right]}{L_x^{pl} L_y^{pl} (m_{y_1} + m_{y_2} - 1) (m_{x_1} + m_{x_2} - 1)} \\
&\quad * \left[ \left( \frac{2x^{pz} + L_x^{pz}}{L_x^{pl}} \right)^{m_{x_1} + m_{x_2} - 1} - \left( \frac{2x^{pz} - L_x^{pz}}{L_x^{pl}} \right)^{m_{x_1} + m_{x_2} - 1} \right] \\
&\quad * \left. \left[ \left( \frac{2y^{pz} + L_y^{pz}}{L_y^{pl}} \right)^{m_{y_1} + m_{y_2} - 1} - \left( \frac{2y^{pz} - L_y^{pz}}{L_y^{pl}} \right)^{m_{y_1} + m_{y_2} - 1} \right] \right\}
\end{aligned}$$

## Chapter 4: Experimental Setup

This section describes the two main test setups used throughout this study to validate the models and a new test setup is proposed to further the research.

### 4.1 NASA Validation Case

This test setup and experimentation was performed by Heatwole at NASA [1,64]. This test consisted of a rectangular, simply supported, aluminum test panel flush mounted into the floor of a windtunnel test chamber and an acoustic enclosure mounted below the panel and outside the test chamber. Once the windtunnel reached constant airspeeds, the sound pressure level radiated by the panel was measured both below, and outside of the test chamber in an acoustic enclosure using microphones and an accelerometer attached to the center of the panel [64]. This vibrational data was originally used to validate Rocha's model for a TBL excitation [1], among others. Figure 6 shows a depiction of the experimental test setup used by Heatwole.

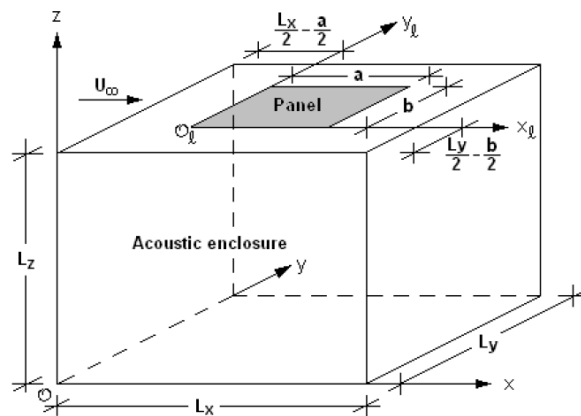


**Figure 6:** Experimental test setup used by Heatwole [1,64].

In the context of this research, this test case was used to prove that a TBL excitation on a real aircraft panel produces the same results as the initial coding of Rocha's model. By using the same panel parameters and flight conditions from Heatwole's research, as seen in Table 1, the same results were obtained as Rocha's research [1,64]. Figure 7 was produced using the new Matlab code generated for this research. This can be compared to Rocha's results as seen in Figure 8, to verify the correct functionality of the code and the values it produces.

**Table 1:** NASA Experimental Test Parameters [64].

Variable	Description, Units	Value
$a$	Panel Length [m]	0.46
$b$	Panel Width [m]	0.33
$\rho_p$	Panel Density [ $\text{kg m}^{-3}$ ]	2800
$h_p$	Panel Thickness [m]	0.0048
$\nu_p$	Poisson Ratio	0.3
$E_p$	Panel Elasticity Modulus [Pa]	$6.5 * 10^{10}$
$\zeta_p$	Damping Ratio	0.01
$\rho$	Density of Air [ $\text{kg m}^{-3}$ ]	1.225
$U_\infty$	Free Stream Velocity [ $\text{m s}^{-1}$ ]	35.8
$U_\infty$	Free Stream Velocity [Knots]	69.6
$U_c$	Convective Velocity [ $\text{m s}^{-1}$ ]	$0.65U_\infty$
$\alpha_x/\alpha_y$	Empirical Parameters	0.115/0.7
$c_o$	Speed of Sound [ $\text{m s}^{-1}$ ]	340
$Re_x$	Reynolds Number	$4.27 * 10^7$

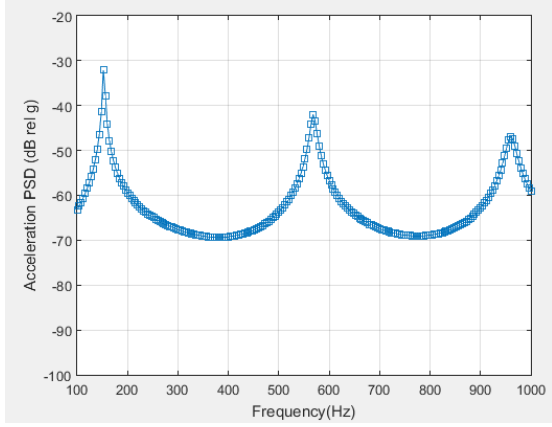


**Figure 7:** Predicted results as calculated by new Matlab code for the acceleration PSD given the NASA experimental test setup [64].

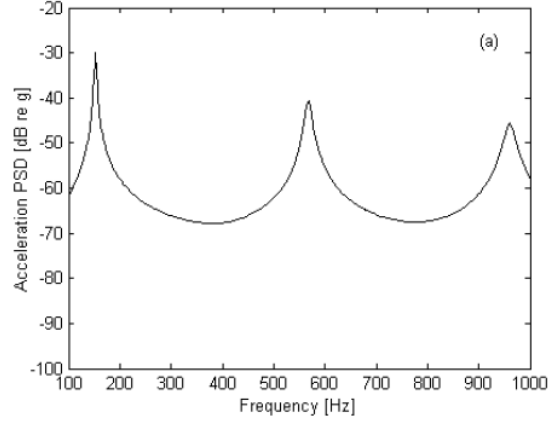


**Figure 8:** Predicted results as calculated by Rocha for the acceleration PSD given the NASA experimental test setup (same results used to validate Rocha's Model given a TBL excitation) [1,64].

For these plots the reference power spectral density of the external pressure field ( $S_{ref}$ ) is assumed to be a constant defined as:

$$S_{ref} = 7.5 * 10^{-5} \lambda^2 \rho^2 U_{\infty}^3 \delta^* \quad (65)$$

where  $\lambda = 3$  (a constant)

This approximation for the reference power spectral density of the external pressure field is accurate for the range of frequencies used here. However, for the other results obtained throughout this study, a frequency dependent model is used. Efimtsov's model has been used for the other simulations and studies [65]:

$$S_{ref}(\omega) = 2\pi\alpha_1 U_T^3 \rho^2 \delta \frac{\beta_1}{(1 + 8\alpha_1^3 Sh^2)^{\frac{1}{3}} + \alpha_1 \beta_1 Re_T \left(\frac{Sh}{Re_T}\right)^{\frac{10}{3}}} \quad (66)$$

where its variables can be defined as follows:

$$U_T = U_\infty \sqrt{\frac{C_f}{2}} \quad (67)$$

$$C_f = 0.37(\log_{10} Re_x)^{-2.584} \quad (68)$$

$$Re_x = \frac{U_\infty x}{\nu} \quad (69)$$

$$\delta = 0.37x Re_x^{-\frac{1}{5}} \left[ 1 + \left( \frac{Re_x}{6.9 * 10^7} \right)^2 \right]^{\frac{1}{10}} \quad (70)$$

$$\beta_1 = \left[ 1 + \left( \frac{Re_{To}}{Re_T} \right)^3 \right]^{\frac{1}{3}} \quad (71)$$

$$Re_{To} = \frac{\delta U_T}{\nu} \quad (72)$$

$$Re_T = \frac{\delta U_T}{\nu_w} \quad (73)$$

$$\nu_w = \nu \frac{\rho}{\rho_w} \left( \frac{T_w}{T} \right)^r \quad (74)$$

$$\rho_w = \rho \left( \frac{T}{T_w} \right) \quad (75)$$

$$T_w = T \left( 1 + r \frac{k-1}{2} N_{Ma}^2 \right) \quad (76)$$

$$Sh = \frac{\omega \delta}{U_T} \quad (77)$$

In which the constants are  $\alpha_1 = 0.01$ ,  $r = 0.89$ , and  $k = 1.4$ .

## 4.2 DLR Experimental Test Setup

The majority of the experimental validation done throughout this study used data acquired from the panel apparatus at DLR in Braunschweig, Germany. Their apparatus has been previously tested and validated in both wind tunnel, and loud speaker excitation testing [41,48]. The test setup for this research is in its vertical configuration as seen in Figure 9. The panel's boundary conditions are designed to replicate that of an aircraft (in between simply supported and clamped boundary conditions). The test setup is used in airflow tests and, as such, is flush mounted with the plywood base on one side, and a complex mounting system on the other side, as seen in Figure 9. The specifics of the mounting system are defined in Misol's and Hu's work [41,48].

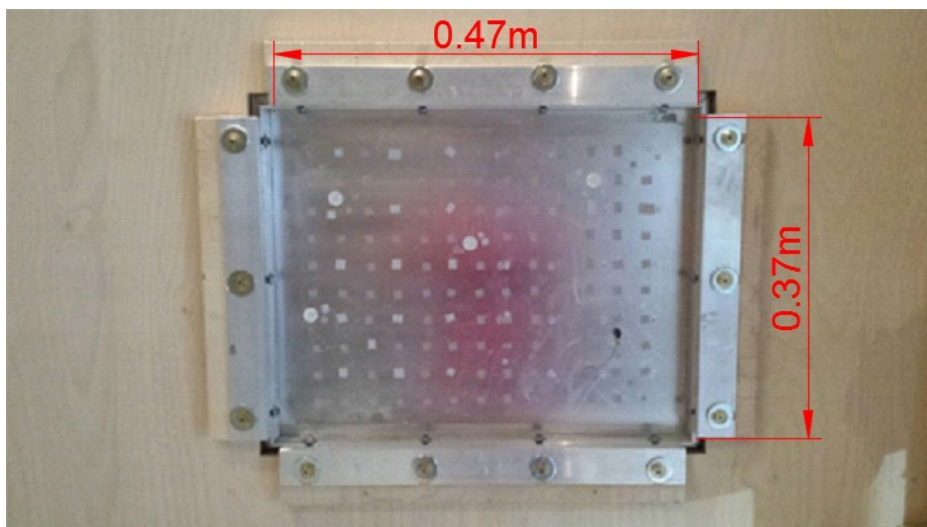


**Figure 9:** Front view of the DLR test setup.

The test setup can be excited with several different devices, such as, air flow in the DLR windtunnel, DLR's loudspeaker array, an impact hammer, and a piezoelectric actuator, as seen in Figure 10.

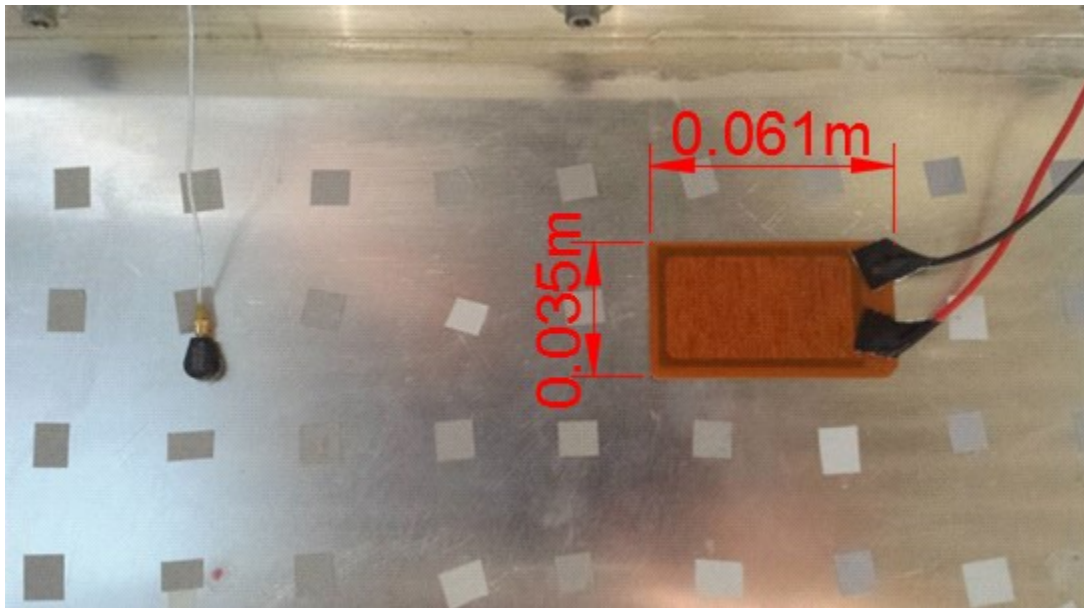


**Figure 10:** Excitation and monitoring system of the DLR test setup, using a piezoelectric patch and an accelerometer.

### 4.3 Carleton University Experimental Test Setup

The final test setup is newly designed at Carleton University, and has been constructed to allow similar experimentation as the one at DLR, with a few modifications. The test setup has been designed to be smaller, in order to fit in the available semi-anechoic chamber, and to have interchangeable panels under different boundary conditions. The test setup consists of a plywood base, for lightweight construction, with the plywood connected to both sides of an aluminum panel using steel brackets. These steel brackets ensure minimal panel mode interactions between the aluminum panel and the plywood base (eliminating the presence of the natural frequencies of the plywood in the panel response of the aluminum panel). The entire system is clamped to the

side of an open steel table frame to hold the structure and prevent any enclosure effects due to rebounding sound waves. By orienting the system in a vertical position, the sound waves are able to propagate away from the panel, towards the anechoically treated side wall, not towards the untreated floor. The front and rear views of the constructed test setup can be found in Figure 11 and Figure 12 respectively.

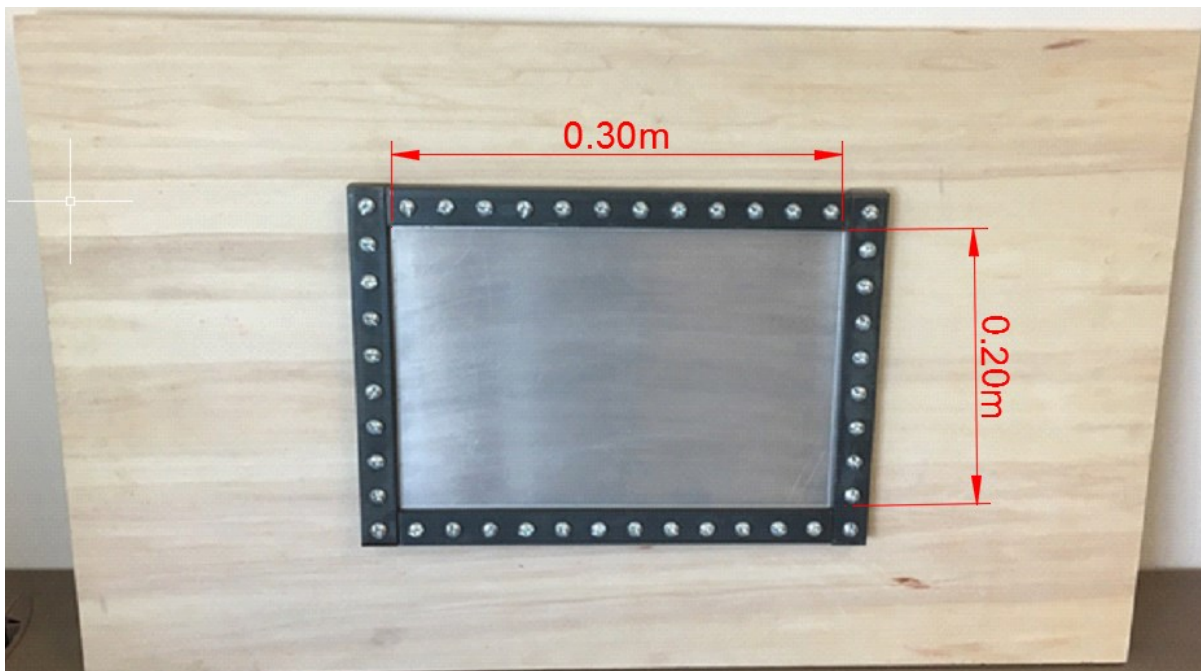


**Figure 11:** Front view of the constructed Carleton University test setup.



**Figure 12:** Rear view of the constructed Carleton University test setup.

The designed test setup is built to replicate clamped boundary conditions by bolting a piece of aluminum in between the steel clamps. The panel size is equal to the distance between steel clamps. A panel can be designed that mounts to the test setup in the same manner, replicating simply supported boundary conditions. Robin et al. summarized different experimental techniques to represent simply supported boundary conditions and even proposed his own experimental technique [47]. Figure 13 contains their summarized diagrams of different experimental approaches.

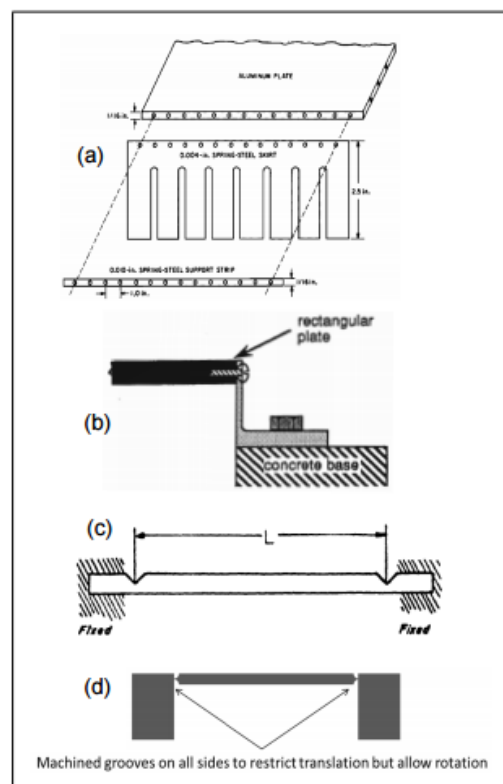


**Figure 13:** Robin's [47] summarized diagram of experimental setups that represent simply supported boundary conditions by: (a) Ochs [43] (b) Champoux [44] (c) Hoppmann [45] and Barnard [46]

The proposed test setups are very difficult to construct due to the thickness of the aircraft panel being replicated. The panel to be analyzed is 0.04 inches representing a thick aircraft panel, which makes Och's and Champoux's setups difficult because they require a hole to be drilled on

the side and the panel is too thin for such a method of construction. The easiest setup, is Hoppmann's, as seen in Figure 13(c) [45]. The size of the panel is determined by the distance in between the notches. Hoppmann suggests that the depth of the cuts are required to be at least 80% of the thickness of the material to best mimic simply supported boundary conditions. Leaving 20% of the material, makes the panel boundaries unable to translate, but the rotational stiffness is minimal, which means it is able to rotate freely. To produce this type of panel, a vacuum table was used on a CNC machine to route the perimeter of the panel.



**Figure 14:** A look at the 80% thickness cut in an aluminum panel to represent simply supported boundary conditions.

The test setup has been constructed. In future work, the panel can be analyzed to determine how close the test setup recreates the effects of simply supported boundary conditions. The test setup used to determine which model is better at predicting the acceleration PSD due to different excitations for a panel with simply supported boundary conditions. This will be an advancement from the DLR test setup because it currently can only be used to test Berry's model. Appendix A contains orthographic drawings of the Carleton University test setup.

## **Chapter 5: Results**

There are three main sections of this research. The first is a panel parameter study which uses Rocha's model to determine which panel parameter is most effective at reducing the acceleration PSD, and to design a tool that determines the optimal panel configuration for given flight conditions. The second section uses the test setup at DLR to compare with Rocha's and Berry's models for different excitations. The final section determines the optimal piezoelectric patch placement to replicate the panel response due to a TBL excitation.

### **5.1 Panel Parameter Sensitivity Study and Panel Length Optimization**

A sensitivity study is performed on seven panel parameters to determine which parameter is most effective at reducing the acceleration PSD in select octave bands. The parameters were varied individually while maintaining the other variables at their initial values, and the changes in the integrated acceleration PSD over each of the octave bands were analyzed. In the present study, no constraints have been considered (one parameter relative to another), in order to determine the general trends when optimizing each of the seven individual parameters. Future work could consider these constraints. The following octave bands (in the human hearing range) have been analyzed: 89.1-178 Hz, 178-355 Hz, 355-708 Hz and 708-1410 Hz. The sensitivity study was run for seven parameters: thickness, material density, panel width and length, elastic modulus, Poisson's ratio and damping ratio. Table 2 contains the initial panel parameters used in the sensitivity study (the same ones used in the NASA research [54]) and Figure 15 to Figure 18 contain the sensitivity studies, for each of the octave bands.

**Table 2:** Initial panel parameters for optimization.

Variable	Value
Length	0.46 m
Width	0.33 m
Thickness	0.0048 m
Elasticity Modulus	$6.5 \times 10^{10}$ Pa
Density	$1.225 \text{ kg/m}^3$
Poisson's Ratio	0.3
Damping Ratio	0.01

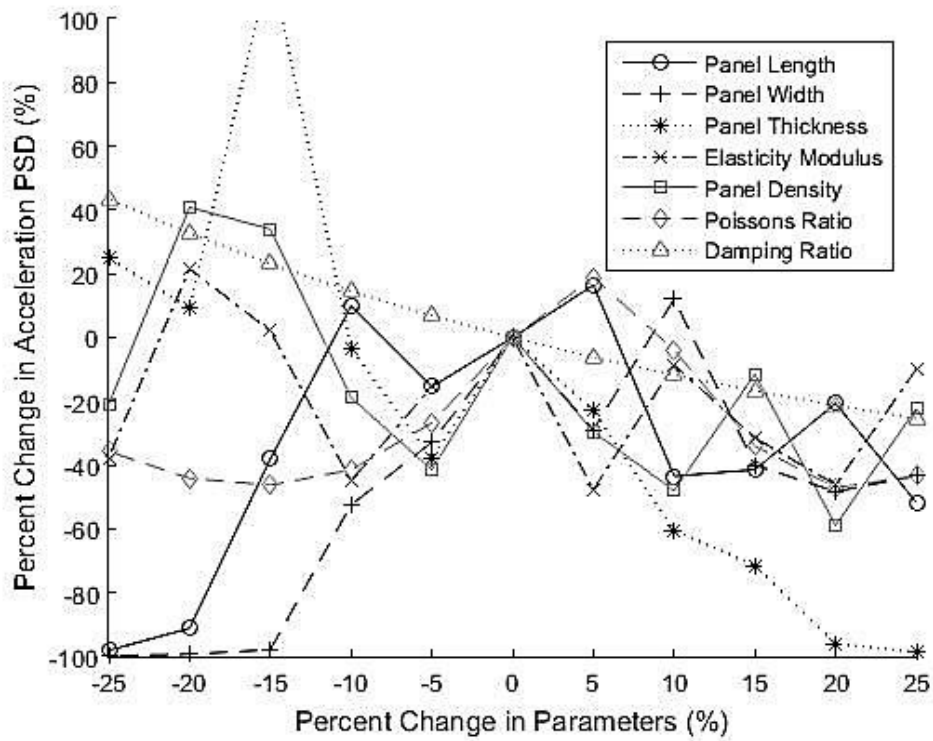


**Figure 15:** Percent change in acceleration PSD versus percent change in panel parameter for octave 89.1-178 Hz with limited Y-axis extents.

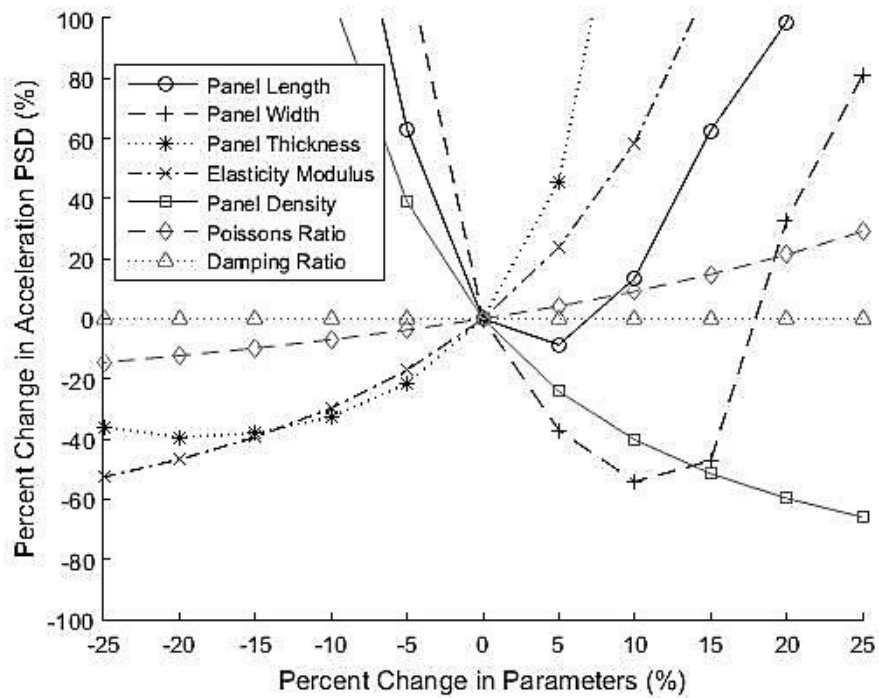


**Figure 16:** Percent change in acceleration PSD versus percent change in panel parameter for octave 178-355 Hz with limited Y-axis extents.

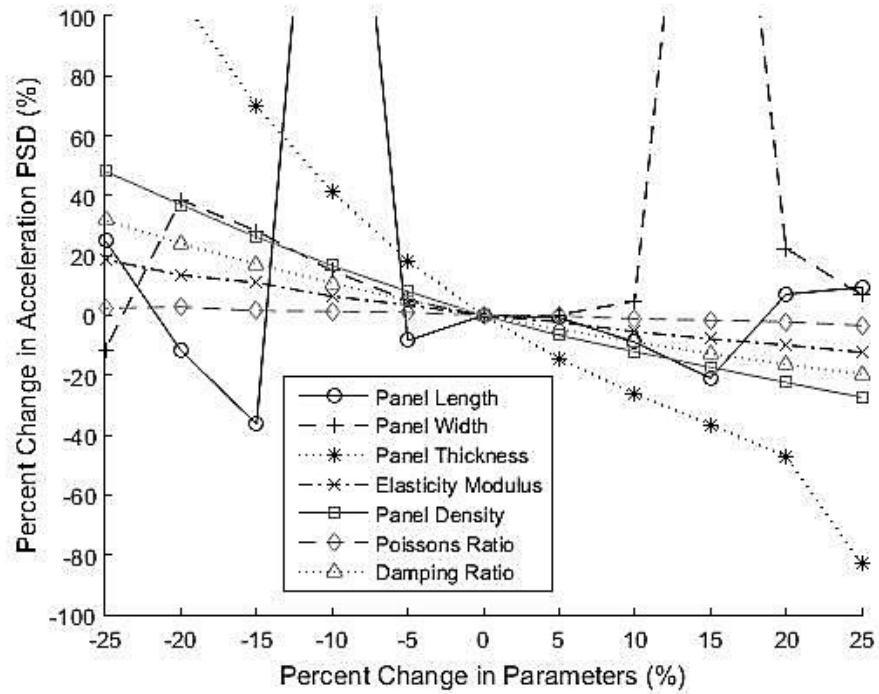


**Figure 17:** Percent change in acceleration PSD versus percent change in panel parameter for octave 355-708 Hz with limited Y-axis extents.

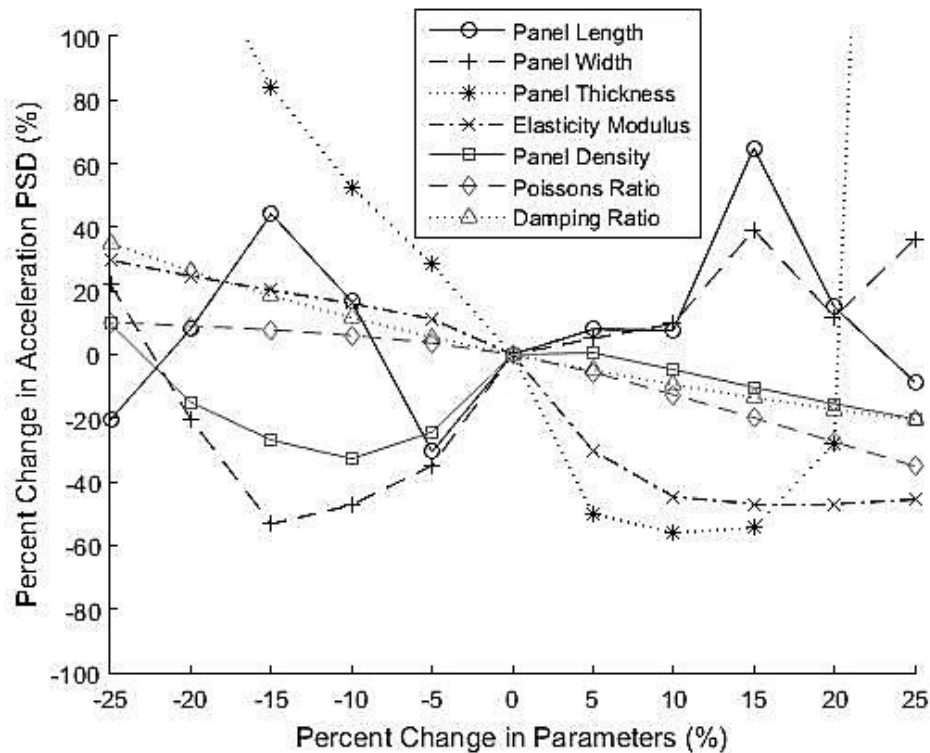


**Figure 18:** Percent change in acceleration PSD versus percent change in panel parameter for octave 708-1410 Hz with limited Y-axis extents.

It can be seen from Figure 15 that there is very low correlation between change in panel parameters and change in acceleration PSD at frequencies, between 89.1-178 Hz. This could be caused by the low number of panel modes existing at low frequencies. This can also be seen from the convergence criteria [19], as frequency decreases, the required panel modes to achieve convergence decreases. When the parameters are modified at these low frequencies, the convergence test results in values less than one. Therefore, the octave band 89.1-178 Hz is not to be considered in this analysis when determining which panel parameter is most sensitive to changing the acceleration PSD.

As shown in Figure 16 to Figure 18, both the panel width and length have fluctuating values. These fluctuations are believed to occur because the panel width and length are main components in the calculation of  $S_{tbl}(\omega)$ . The variables are located within sinusoidal functions, and therefore, the change in these parameters are non-linear. Since, these parameters cannot be defined by a simple trend, they are not the most sensitive at reducing the overall acceleration PSD.

It was found that the two parameters most effective for reducing the average acceleration PSD, within the different octave bands, are panel thickness and panel density, as these two parameters have the steepest slopes. As the thickness is increased, the higher frequency noise is reduced, as expected. However it has less effect on the lower frequency signals. Even though panel density has more gradual slopes when compared to panel thickness, the trend is more consistent across all of the analyzed octave bands. Hence, it is likely that acceleration PSD is most sensitive to the change in panel density and thereby reducing the overall noise across the human hearing range, whereas panel thickness may be most sensitive at reducing noise at certain octave bands.

The analysis was then modified to determine the optimal panel parameters resulting in the smallest average acceleration PSD over the octave band. The analysis is used to optimize each of the seven parameters individually, and concurrently. Since the general trend of the sensitivity studies predicts the minimum acceleration PSD is reached when both the panel thickness and density are maximized to the upper constraint, optimizing these parameters individually simply results in the upper constraint. Therefore, it is of more interest to determine if there is a correlation between the octave band and the panel length.

The optimization problem defined for this study can be defined mathematically as:

Minimize:

$$f(x) = \int_{\omega_L}^{\omega_U} S_{ww}(\omega) \quad (78)$$

Where  $\omega_L$  is the smallest frequency in the specific octave band being analyzed and  $\omega_U$  is the largest frequency in the octave band. This is subject to no equality or inequality constraints to simplify the optimization (no  $g_i(x) \leq 0$  and  $h_j(x) = 0$ ). The only variable being optimized is the overall panel length (in meters) and it is being optimized within the following bounds:

$$0.05 \leq a \leq 2.00 \quad (79)$$

The initial starting point on the optimization is at  $a = 1.5m$ . Figure 19 shows the optimal panel length at the center frequency of different octave bands, and compares these values to the calculated flexural wavelength, convective wavelength and acoustic wavelength, at the same frequencies [66]. These wavelengths can be defined as follows [66]:

$$\text{Flexural Wavelength} = \sqrt{\frac{1.8h_p C_L}{f}} \quad (80)$$

$$\text{Convective Wavelength} = \frac{U_c}{f} \quad (81)$$

$$\text{Acoustic Wavelength} = \frac{c_o}{f} \quad (82)$$

Where  $C_L$  is the velocity of propagation of longitudinal waves within the material defined as:

$$C_L = \sqrt{\frac{E_p}{\rho_p(1 - \nu_p^2)}} \quad (83)$$

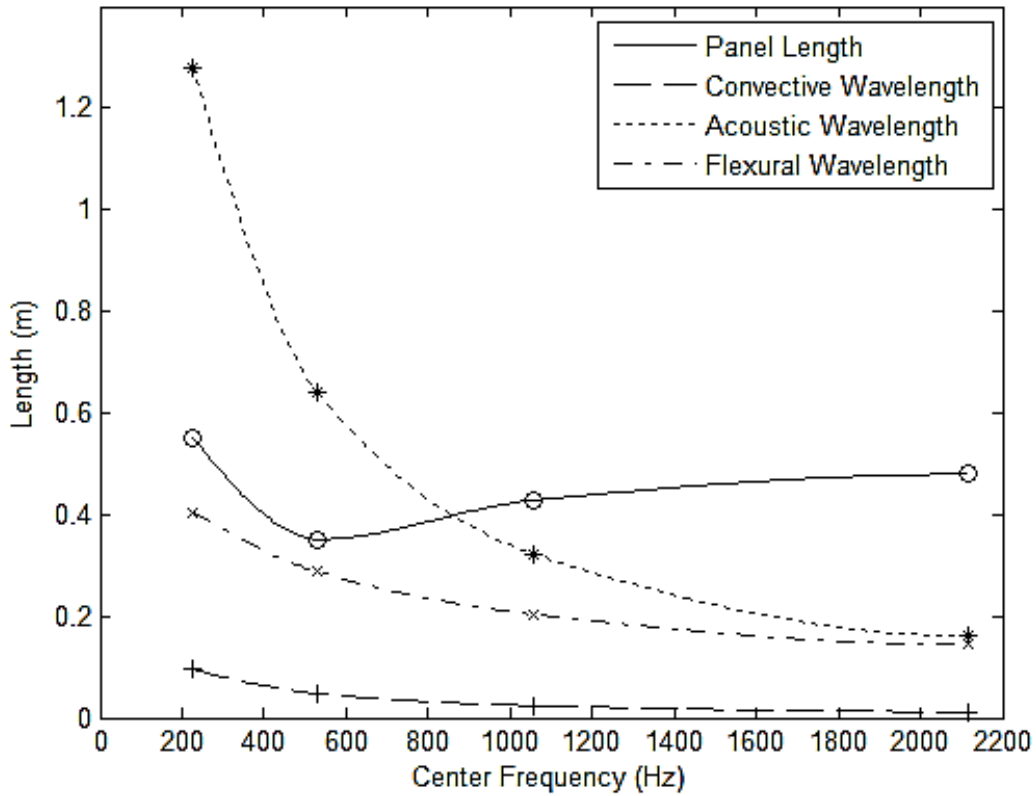


**Figure 19:** Optimal panel length at the center frequency of different octave bands that result in a local minimum average acceleration PSD compared to the calculated flexural wavelength, convective wavelength and acoustic wavelength [66].

It was hypothesized that the optimal panel length could be related with the flexural wavelength, convective wavelength and acoustic wavelength; however, Figure 19 does not support this for frequencies higher than 355-708 Hz octave band. This is because the optimization routine currently finds local minimums in the constrained space, rather than the

global minimum. It also shows that by averaging over an entire octave band it becomes difficult to see the exact correlation between the panel length and the frequency.

Therefore, two modifications to this approach were taken to gain a better understanding of the relationship between frequency and optimal panel length. The first change was modifying the optimizing routine, to have a better chance at predicting that the overall global minimum was being determined, and to ensure the resulting panel length was not the location of a local minimum occurring at some multiple of the wavelength. The second modification was calculating the optimal panel length, for individual frequencies, instead of over an entire octave band. This allows for a more detailed curve to be plotted for length versus frequency. The optimization problem defined for this study can be defined mathematically as:

Minimize:

$$f(x) = S_{ww}(\omega) \quad (84)$$

Here only a single frequency is being optimized for at a time. This is subject to no equality or inequality constraints to simplify the optimization (no  $g_i(x) \leq 0$  and  $h_j(x) = 0$ ). The only variable being optimized is the overall panel length (in meters) and it is being optimized within the following bounds:

$$0.05 \leq a \leq 2.00 \quad (85)$$

This optimization routine is run multiple times at different starting points of panel length to better approximate the global minimum. Figure 20 shows the result of this new optimization study, over the first two octave bands previously investigated.

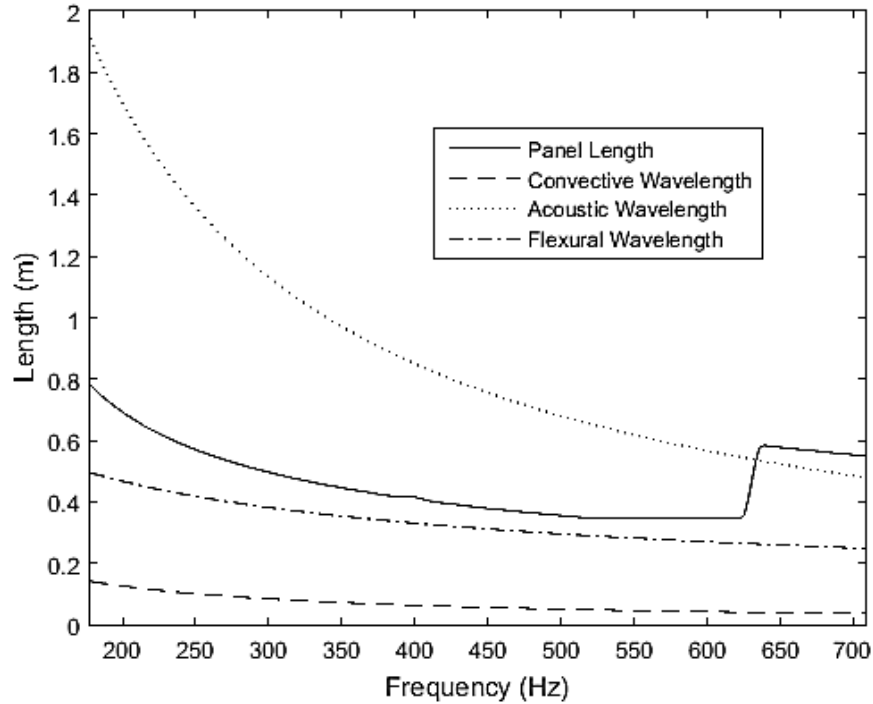


**Figure 20:** Optimal panel length at individual frequencies that result in a global minimum average acceleration PSD compared to the calculated flexural wavelength, convective wavelength and acoustic wavelength for two octave bands (up to 700 Hz).

Figure 20 shows there are additional panel lengths that result in local minimum acceleration PSDs and that the optimal panel length, resulting in the true global minimum, follows the same exponential decay as the flexural wavelength, convective wavelength and acoustic wavelength. From 178 Hz to 500 Hz the global minimum acceleration PSD is found at panel lengths that follow the expected exponential decay. From 500 Hz to 625 Hz the optimization routine levels off at the lower bound of the design space for the optimization routine. The lower bound was decreased as low as possible while running this routine. The lower

bound cannot be further decreased because of the convergence test. If the panel length is set too small, the convergence test results in a very small number, meaning a few panel modes are used to calculate the acceleration PSD. This causes inaccurate values to be predicted for the acceleration PSD and skews the optimization data. From 625 Hz to 708 Hz a shift in the plot is observed. Since the true global minimum would be found below the lower bound of the integration, the optimizing routine finds a local minimum which is smaller than the acceleration PSD at the lower bound. The local minimum found is approximately equal to two times the expected global minimum. Therefore, there are local minimums at multiples of the optimal panel length. Figure 21 shows the result of the optimization study, over four octave bands.

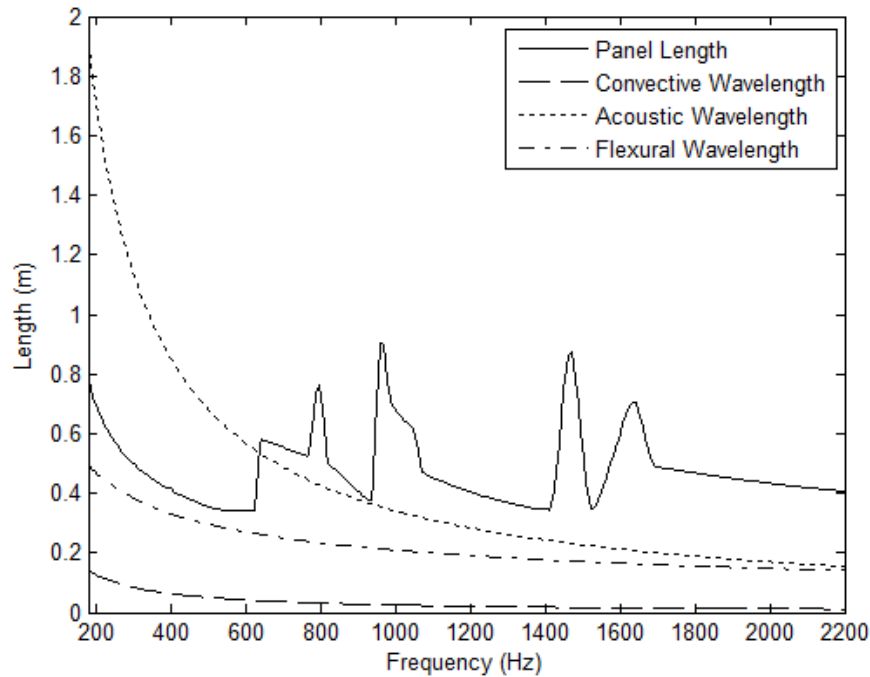


**Figure 21:** Optimal panel length at individual frequencies that result in a global minimum average acceleration PSD compared to the calculated flexural wavelength, convective wavelength and acoustic wavelength for four octave bands.

Figure 21 is a continuation of Figure 20, for higher frequencies. From Figure 21, it can be seen that, at certain frequencies, the optimizing model does not find global minimums at lengths

correlating to the convective, acoustic or flexural wavelengths. These regions coincide with the peaks in the acceleration PSD for the lengths in this study (these same peaks are observed in Rocha's earlier work, associated to the "Validation Case 2" in Figure 5 [1]. At these regions, the peaks shift as the panel length changes making it difficult to determine an optimal panel length. It is found that the length at which the peak shifts the most, does not converge to the length that has minimized the amplitude of the peak. However, by moving away from these regions, the lengths follow the same exponential decay as the convective, acoustic and flexural wavelengths at multiples of the expected optimal panel lengths.

## **5.2 Analytical Model Validations for Different Excitations**

Using the experimental setup at DLR, Berry's, Rocha's and modified Berry's models were compared and validated for three different excitations: an impact hammer force, a TBL excitation and a piezoelectric patch excitation.

### **5.2.1 Impact Hammer**

The first goal was to use the impact hammer to strike the panel at one location and measure the acceleration using a miniature (<1g) single axis piezoelectric accelerometer at a different location on the panel. The benefit of this test is that it is accurate and relatively simple to complete multiple configurations of hammer and accelerometer locations.

The first step was to compare Rocha's model to Berry's model. Therefore, boundary conditions of a simply supported panel were used in Berry's model and the same panel parameters were given to each code. Table 3 lists the panel parameters of the test panel used and Figure 22 shows the resulting acceleration PSD for a given impact excitation for each of the models, and compares it to simulation results obtained from Ansys. Berry's model cannot accept

infinity for the translational stiffness constant, therefore, a value of  $5 * 10^7$  was used as per Berry's original paper [21].

**Table 3:** Physical properties of the test panel.

Variable	Description, Units	Value
a	Panel Length [m]	0.47
b	Panel Width [m]	0.37
$\rho_p$	Panel Density [ $\text{kg m}^{-3}$ ]	2800
$h_p$	Panel Thickness [m]	0.0011
$\nu_p$	Poisson Ratio	0.3
$E_p$	Panel Elasticity Modulus [Pa]	$6.5 * 10^{10}$
$\zeta_p$	Damping Ratio	0.01
$N_x$	Panel Longitudinal Tension [ $\text{N m}^{-1}$ ]	0
$N_y$	Panel Lateral Tension [ $\text{N m}^{-1}$ ]	0

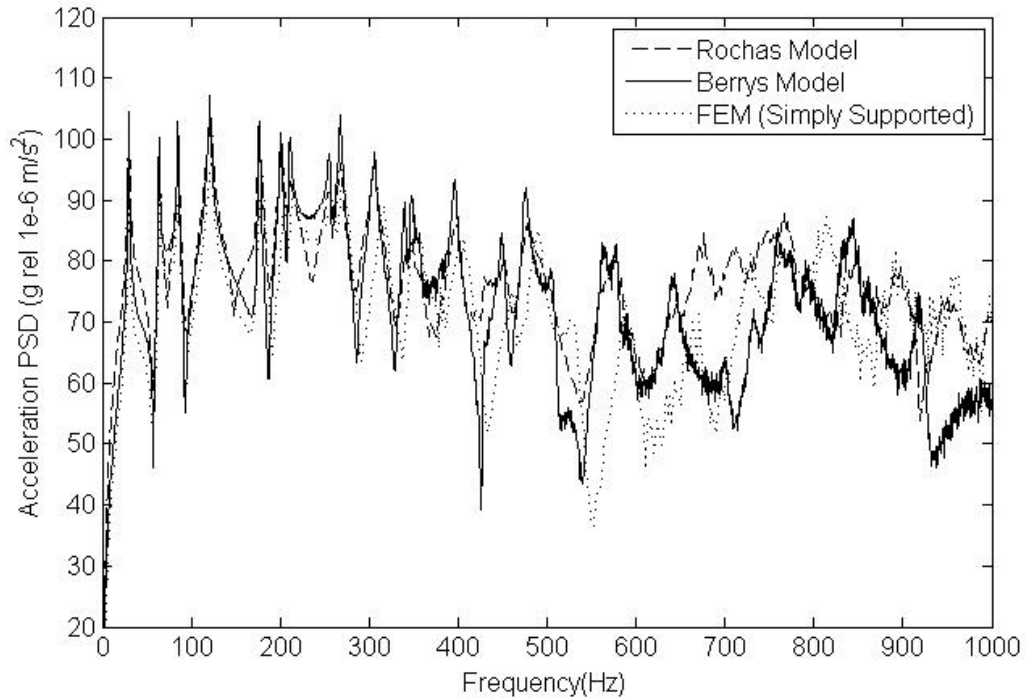


**Figure 22:** Comparison of acceleration PSD results for a panel with simply supported boundary conditions at a point  $x = 20.6$  cm and  $y = 21.6$  cm, with a point force applied at  $x = 7.7$  cm and  $y = 3.8$  cm for three different models.

Figure 22 shows that the models predict the same general shape for the selected acceleration PSD for a given point force excitation. However, there are two main differences in the outputs of the models: the magnitudes of the peaks are different, and at higher frequencies, the models appear to disagree. The difference in the magnitudes of the peaks is likely due to the way the damping is entered into each model. In Rocha's model, the damping is defined using the damping matrix, whereas in Berry's model the effects of the panel's damping is included as an imaginary component in the stiffness matrix. This might be the reason why Berry's model under predicts the amount of damping present when compared to Rocha's model and finite element method (FEM) results. The divergence of Berry's model occurs around 600 Hz due to the number of panel modes used at these high frequencies. An erroneous appearance of a singular matrix appears in Berry's model when the mode number is very high  $(m, n) \geq (10, 10)$ . This error can be mitigated if the frequencies of interest are small, or the panel's thickness is increased, requiring less panel modes. However, it appears that by selecting polynomial trial functions, the frequency range that can be calculated is severely limited.

The next step was to check Berry's model given "free" boundary conditions. The rotational and translational stiffness constants were set to zero and the acceleration PSD at a single point was compared to the results given from the Ansys model. The results can be seen in Figure 23.

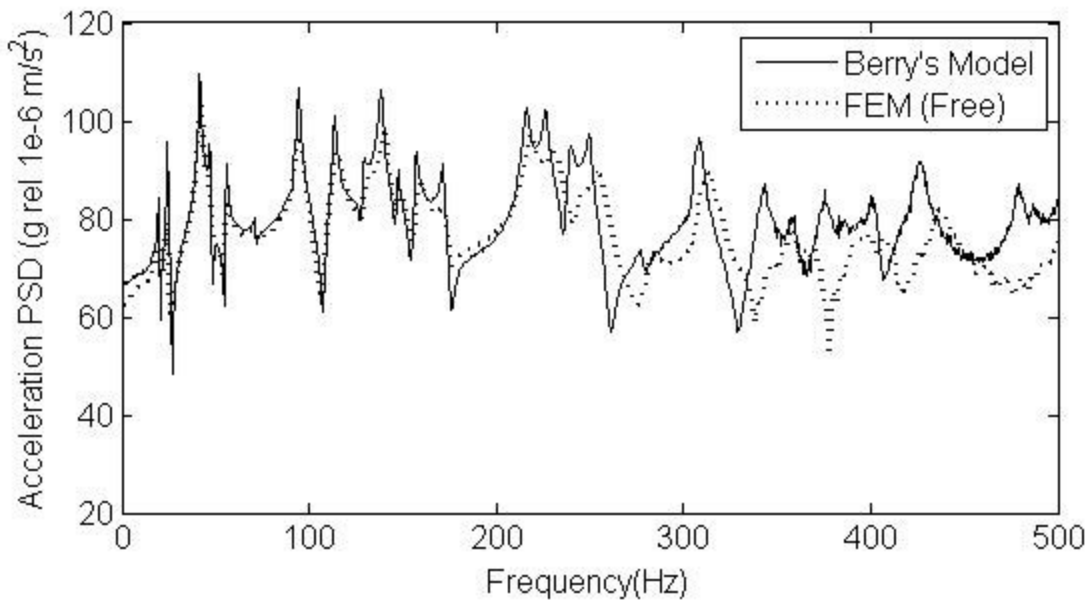


**Figure 23:** Comparison of acceleration PSD results for a panel with free boundary conditions at a point  $x = 20.6$  cm and  $y = 21.6$  cm with a point force applied at  $x = 7.7$  cm and  $y = 3.8$  cm for two different models.

The third step was to gather experimental data. Using the test setup at DLR, an accelerometer was placed on the panel using wax, and the panel was struck using an impact hammer [41,48]. The location of the impact hammer and accelerometer were measured, and both the force data and the acceleration data were recorded. The accelerometer data was used as the experimental PSD values and were compared to the results given by Berry's model, using the force data from the impact hammer as the input to the model. This test enabled the translational and rotational stiffness constants ( $c$  and  $k$ ) to be found for this particular test panel. This was done by varying the values of  $c$  and  $k$  until the predicted plot most accurately matched the experimental data, as seen in Figure 24 (each new test panel setup would need to be tested similarly to determine their values of  $c$  and  $k$ ):

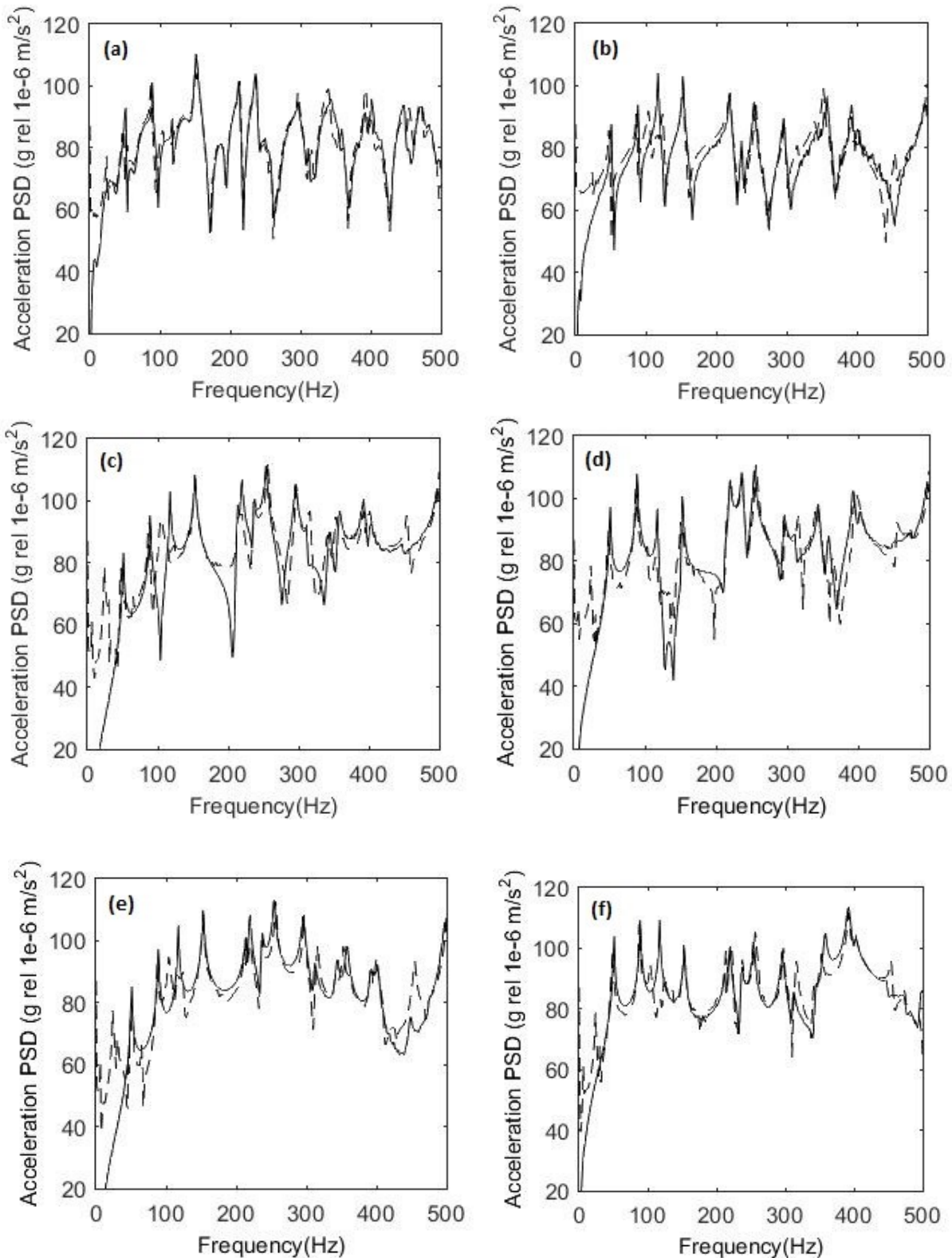


**Figure 24:** Comparison of predicted (solid line) vs. experimental (dashed line) of acceleration PSD results for a panel with arbitrary boundary conditions at: (a) measured at (M):  $x = 5.4 \text{ cm}$ ,  $y = 13.6 \text{ cm}$  and force applied at (F):  $x = 5.4 \text{ cm}$  and  $y = 13.6 \text{ cm}$  (b) M:  $x = 31.2 \text{ cm}$ ,  $y = 32.1 \text{ cm}$  and F:  $x = 31.2 \text{ cm}$  and  $y = 32.1 \text{ cm}$  (c) M:  $x = 31.2 \text{ cm}$ ,  $y = 32.1 \text{ cm}$  and F:  $x = 4.5 \text{ cm}$  and  $y = 3.9 \text{ cm}$  (d) M:  $x = 31.2 \text{ cm}$ ,  $y = 32.1 \text{ cm}$  and F:  $x = 4.2 \text{ cm}$  and  $y = 19.8 \text{ cm}$  (e) M:  $x = 31.2 \text{ cm}$ ,  $y = 32.1 \text{ cm}$  and F:  $x = 4.2 \text{ cm}$  and  $y = 32.2 \text{ cm}$  (f) M:  $x = 31.2 \text{ cm}$ ,  $y = 32.1 \text{ cm}$  and F:  $x = 10.6 \text{ cm}$  and  $y = 26.0 \text{ cm}$

To ensure the model was working accurately over the entire panel, 14 additional hammer and accelerometer locations were measured experimentally. The experimental data was compared to the predicted values and they all resulted in similar plots. This indicated that the model worked over the entire area of the plate (up to 500 Hz) and that the values of  $c$  and  $k$  selected were accurate.

It is important to note that since Berry's model uses polynomial trial functions it takes many more modes to accurately predict the acceleration PSD than Rocha's model. In the convergence equations, in order to get accurate predictions for Berry's model,  $F_{\max}$  is set five times higher than when used for Rocha's model. This means it takes more modes to result in an accurate prediction of the acceleration PSD, being more computationally expensive.

### **5.2.2 TBL Excitation**

The results for Rocha's model and Berry's model were compared to ensure the new derivation of a TBL excitation defined with polynomial spatial functions was correct (modified Berry's model). Rocha's model has been previously verified and compared to actual wind tunnel test data obtained at NASA, and this code has been validated against these results [1,10]. Berry's model was set with simply supported boundary conditions and run for the same flight conditions as Rocha's. Table 4 shows the flow conditions used to predict the TBL over the test panel. Results can be found in Figure 25.

**Table 4:** Flight condition parameters for TBL.

Variable	Description, Units	Value
$\rho_0$	Density of Air [ $\text{kg m}^{-3}$ ]	1.225
$c_0$	Speed of Sound [ $\text{m s}^{-1}$ ]	340
$U_i$	Freestream Velocity [ $\text{m s}^{-1}$ ]	35.8
$U_i$	Freestream Velocity [Knots]	69.6
$U_c$	Convective Velocity [ $\text{m s}^{-1}$ ]	23.3
$M$	Mach Number	0.105
$Re_x$	Reynolds Number	$4.27 * 10^7$

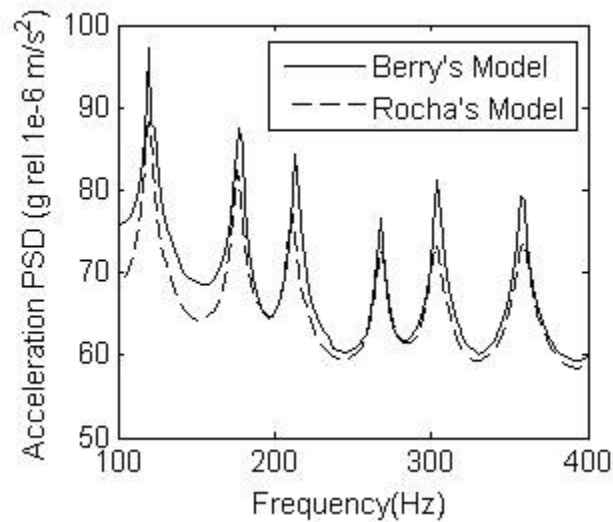


**Figure 25:** Comparison of acceleration PSD results for a panel with simply supported boundary conditions at a point  $x=a/4$  and  $y = b/4$  with a TBL excitation applied.

The accuracy of Berry's model, given a TBL input, is very sensitive to the number of panel modes used. Figure 26 and Figure 27 contain the results when using the same number of panel modes for each of the target frequencies. It shows that each target frequency requires a different number of panel modes to result in an accurate prediction of the acceleration PSD from a TBL excitation. It is shown that it is critical to make a preliminary study on Berry's model in order for reliable results to be obtained. These plots only extend to 400 Hz to highlight these

issues. Table 5 shows how many panel modes are required for both Berry's and Rocha's models at different frequencies.

**Table 5:** Panel modes required for Berry's and Rocha's models for different frequencies.

Frequency [Hz]	Required Panel Modes for Rocha's Model	Required Panel Modes for Berry's Model
100	(3,3)	(6,5)
250	(5,4)	(10,8)
400	(6,5)	(14,11)

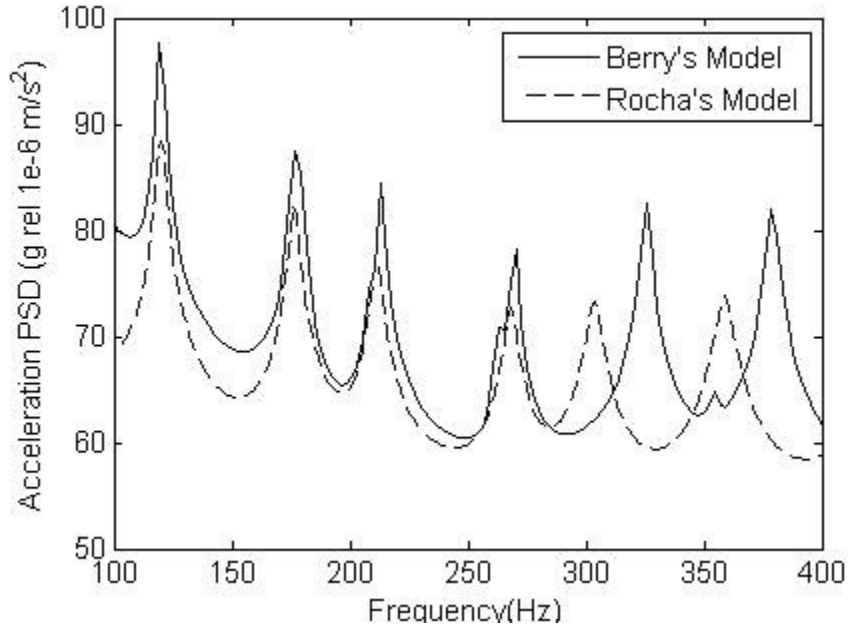


**Figure 26:** Comparison of acceleration PSD results for a panel with simply supported boundary conditions at a point  $x=a/4$  and  $y = b/4$ , with a TBL excitation applied. Each target frequency is calculated with the same constant number of panel modes  $(m, n) = (9,7)$ .

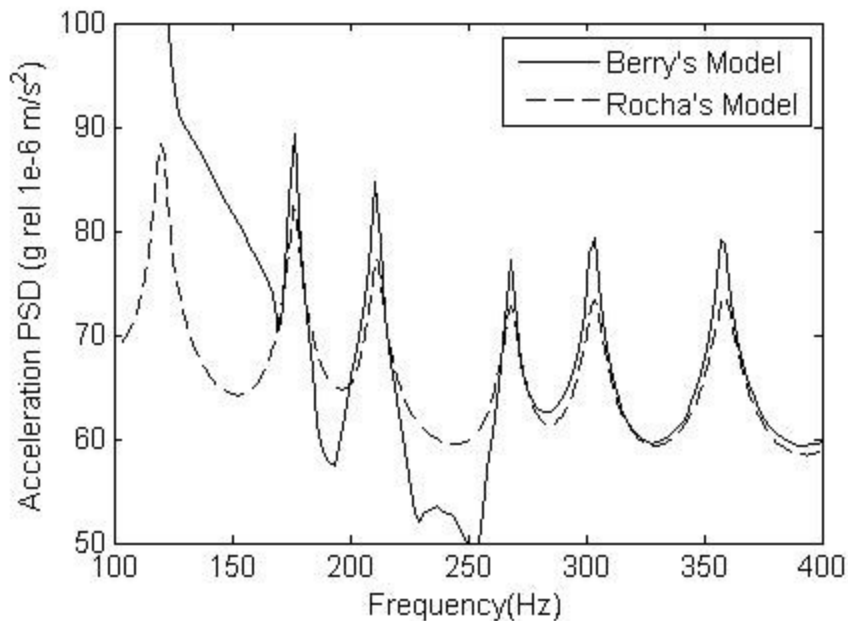


**Figure 27:** Comparison of acceleration PSD results for a panel with simply supported boundary conditions at a point  $x=a/4$  and  $y = b/4$ , with a TBL excitation applied. Each target frequency is calculated with the same constant number of panel modes  $(m, n) = (14,11)$ .

To obtain the results in Figure 25, the convergence test was used to calculate the number of panel modes needed, however, five times the target frequency was used as the input to the test in Berry's model.

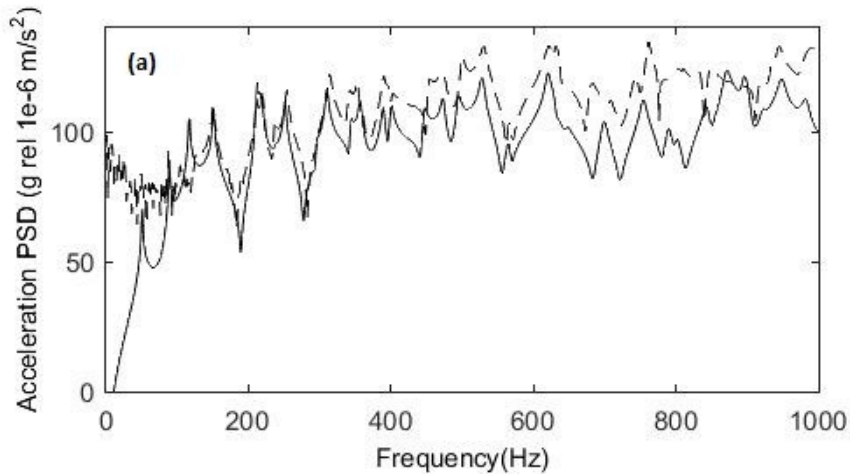
### 5.2.3 Piezoelectric Patch Excitation

A piezoelectric patch has been attached to the test panel using double sided tape at DLR. Although this method is not as accurate as bonding it with glue, it allows for the patch to be moved and multiple tests to be run. The double sided tape has not proven to have a significant impact on the results, as can be seen in Figure 28. The piezoelectric patch is given a frequency sweep with a constant voltage swing and the acceleration measurements taken. Table 6 contains the parameters of the piezoelectric patch used to excite the panel.

**Table 6:** Piezoelectric patch parameters.

Variable	Description, Units	Value
$L_x^{pz}$	Length of piezoelectric patch [m]	0.061
$L_y^{pz}$	Width of piezoelectric patch [m]	0.035
$L_z^{pz}$	Thickness of piezoelectric patch [m]	0.0002
$\rho_{pz}$	Density of piezoelectric patch [ $\text{kg m}^{-3}$ ]	7500
$e_{31}^{pz}$	Effective piezoelectric transverse coefficient (x-direction)	1.02
$e_{32}^{pz}$	Effective piezoelectric transverse coefficient (y-direction)	1.23
$\Delta\phi^{pz}$	Applied voltage peak to peak [V]	8.5
$V^{pz}$	Applied voltage offset [V]	200

Using Charrete and Berry's piezoelectric model for a piezoelectric patch on a panel with arbitrary boundary conditions, the acceleration PSD has been predicted and compared to the experimental data obtained at DLR by the author. The comparison between the predicted response and the actual response is shown in Figure 28. Three additional patches and accelerometer configurations have been tested and exhibit similar results.



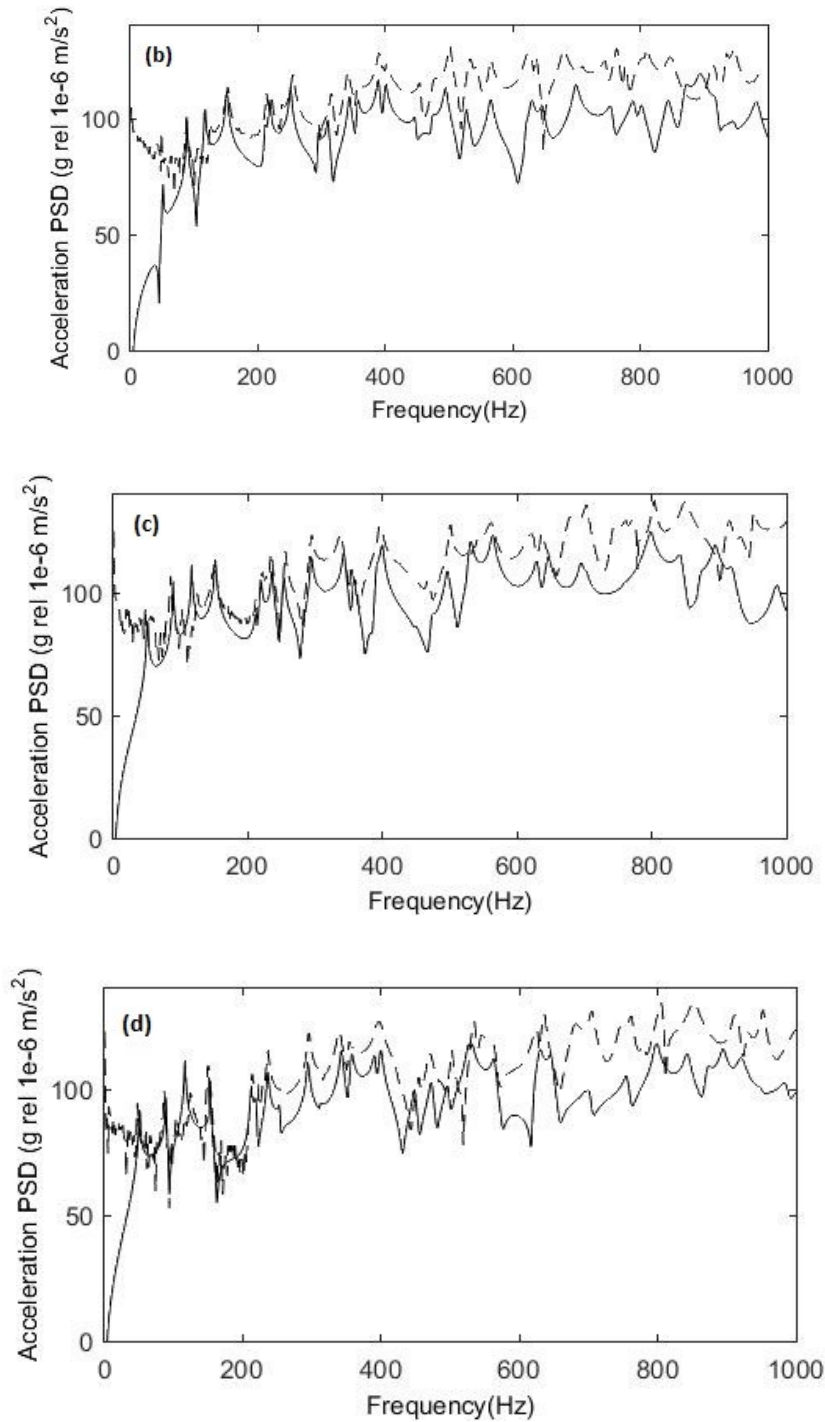


**Figure 28:** Comparison, using Berry’s model, of predicted (solid line) vs. experimental (dashed line) of acceleration PSD results for a panel with arbitrary boundary conditions: (a) measured at (M):  $x = 26.2$  cm,  $y = 8.6$  cm with a piezoelectric actuator excitation applied at (F):  $x = 12.3$  cm,  $y = 7.4$  cm (b) M:  $x = 31.4$  cm,  $y = 26.0$  cm and F:  $x = 12.3$  cm,  $y = 7.4$  cm (c) M:  $x = 31.4$  cm,  $y = 26.0$  cm and F:  $x = 15.5$  cm,  $y = 26.0$  cm (d) M:  $x = 25.5$  cm,  $y = 13.4$  cm and F:  $x = 15.5$  cm,  $y = 26.0$  cm

Figure 28 shows that Berry's model predicts the panel response between 100 and 400 Hz. Below 100 Hz the mounting structure adds additional natural frequencies, and this affects the results. Also, above 400 Hz the polynomial spatial functions do not provide accurate results due to matrices appearing singular. The polynomial spatial functions at high modal numbers start to approach infinity at an exponential rate. The division by such a matrix causes the solution to appear singular. This means the prediction by Berry's model becomes less accurate as the modal number increases. The 400 Hz limiting frequency could be increased if the thickness of the panel is increased. However, between the 100 and 400 Hz range the model appears to accurately predict the panels response due to a piezoelectric patch excitation.

### **5.3 Optimal Piezoelectric Patch Positions to Reproduce TBL Excitation on the Panel**

The final stage of this research is to determine the optimal piezoelectric patch positions to reproduce the response on the panel from a TBL excitation. The piezoelectric patches are given a white noise distribution of frequencies over the frequency range being analyzed. This determines if it is possible to accurately reproduce the response by placing the piezoelectric patches, without requiring complex control signals. It is also important to determine the number of patches required to accurately reproduce the response in order to determine if this approach is feasible in creating a test setup, hence reducing the number of test flights and wind tunnel testing required.

Berry's model has been used to predict the baseline panel response from a TBL excitation, given the same panel and flight conditions as those used on the DLR test setup. Berry's model was then used for a single piezoelectric actuator to compare the theoretical response from a TBL with the response from a piezoelectric actuator. The difference between the two responses is used as the objective function in an optimization routine. The location of the

piezoelectric actuator, in both the span-wise and stream-wise positions, and the voltage swing on the piezoelectric actuator are the design variables in the optimization problem. The optimization problem defined for this study can be defined mathematically as:

Minimize:

$$f(x) = \int_{\omega_L}^{\omega_U} |S_{wwTBL}(\omega) - S_{wwPiezo}(\omega)| \quad (86)$$

Where  $\omega_L$  is the smallest frequency in the specific frequency range being analyzed and  $\omega_U$  is the largest frequency in the frequency range. The optimization is done between 100 – 400 Hz because this is the range where Berry's model, for a piezoelectric actuator excitation, has proven to give accurate results.  $S_{wwTBL}(\omega)$  is the acceleration PSD as calculated by Berry's model from a TBL excitation for the given cruise conditions. The difference between this and the predicted acceleration PSD from a piezoelectric patch excitation ( $S_{wwPiezo}(\omega)$ ) on the panel is used as the objective function. It provides a measure of how well the placement and voltage of a given piezoelectric patch can reproduce the same response on the panel as from a TBL excitation. This optimization is subject to no equality or inequality constraints to simplify the optimization (no  $g_i(x) \leq 0$  and  $h_j(x) = 0$ ). For each piezoelectric patch being optimized 3 variables are being optimized: piezoelectric patch position (x and y) and constant voltage swing across the piezoelectric patch ( $\Delta\varphi^{pz}$ ). These variables have the following bounds

$$0.001 \leq x \leq a \quad (87)$$

$$0.001 \leq y \leq b \quad (88)$$

$$0.001 \leq \Delta\varphi^{pz} \leq 100 \quad (89)$$

This optimization routine is run multiple time with different starting points to ensure a better approximation of the global minimum is obtained. Figure 29 shows the results of this optimization, where the optimal parameters are:  $X = 0.4470$  m,  $Y = 0.1789$  m,  $\Delta\varphi^{pz} = 3.4045$  V.

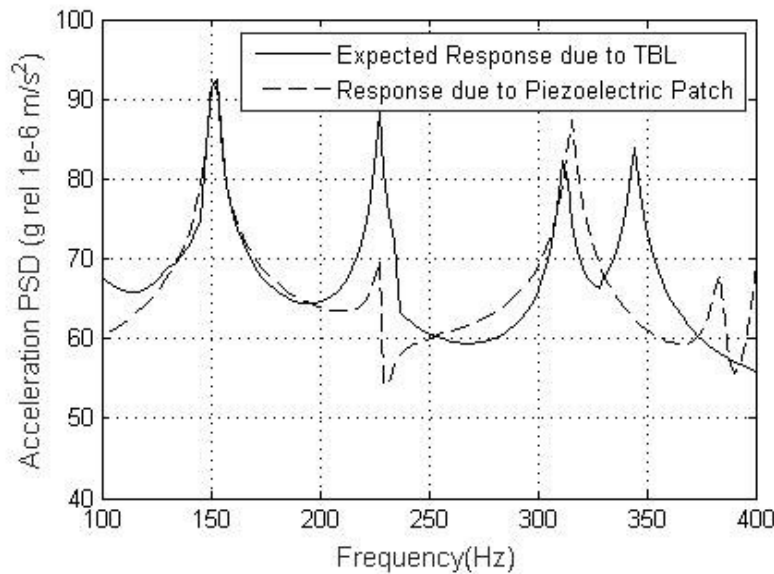


**Figure 29:** Optimal single piezoelectric patch position and alternating voltage potential ( $X = 0.4470$  m,  $Y = 0.1789$  m,  $\Delta\varphi^{pz} = 3.4045$  V) to best reproduce the acceleration PSD of a panel caused by the TBL at constant cruise conditions.

It can be seen from Figure 29 that a single piezoelectric patch is only able to accurately reproduce the first panel mode from a TBL excitation. Therefore, the optimization routine was run again, for two and three piezoelectric actuators on the surface of the panel. Berry's model allowed to incorporate multiple piezoelectric actuators as follows:

$$F_{m_x m_y}^{pz} Total = \sum_{i=1}^n F_{m_x m_y}^{pz} \quad (90)$$

The mass and stiffness matrix of each piezoelectric actuator has to be added to the mass and stiffness matrix of the entire panel. Figure 30 is the result of the optimization for two piezoelectric actuators, where  $X1 = 0.4127$  m,  $Y1 = 0.0211$  m,  $\Delta\phi_1^{pz} = 6.1852$  V,  $X2 = 0.0804$  m,  $Y2 = 0.0513$  m,  $\Delta\phi_2^{pz} = 0.0301$  V is the optimal configuration. Figure 31 is the result of the optimization for three piezoelectric actuators, where  $X1 = 0.3967$  m,  $Y1 = 0.0224$  m,  $\Delta\phi_1^{pz} = 7.0608$  V,  $X2 = 0.1964$  m,  $Y2 = 0.0283$  m,  $\Delta\phi_2^{pz} = 2.1062$  V,  $X3 = 0.0439$  m,  $Y3 = 0.0208$  m,  $\Delta\phi_3^{pz} = 0.0114$  V is the optimal configuration.

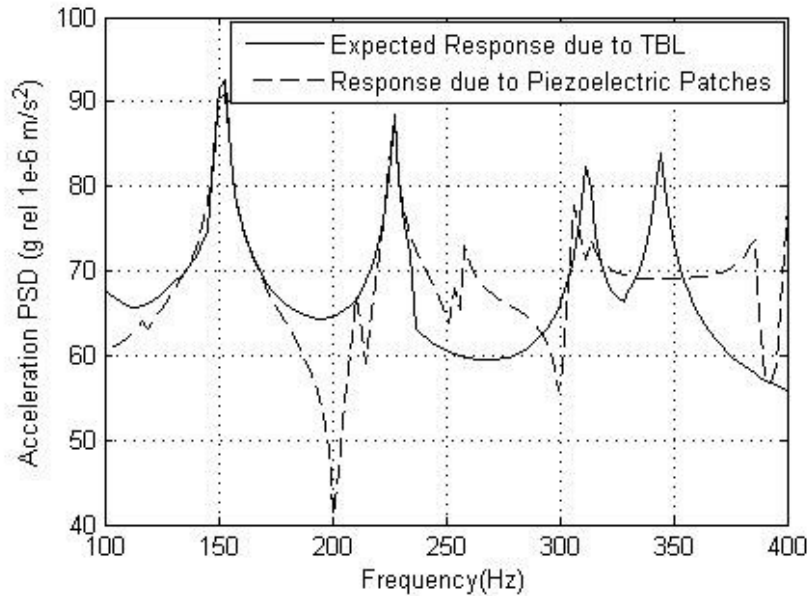


**Figure 30:** Optimal configuration of two piezoelectric patches positions and alternating voltage potentials ( $X1 = 0.4127$  m,  $Y1 = 0.0211$  m,  $\Delta\phi_1^{pz} = 6.1852$  V,  $X2 = 0.0804$  m,  $Y2 = 0.0513$  m,  $\Delta\phi_2^{pz} = 0.0301$  V) to best reproduce the acceleration PSD of a panel caused by the TBL at constant cruise conditions.

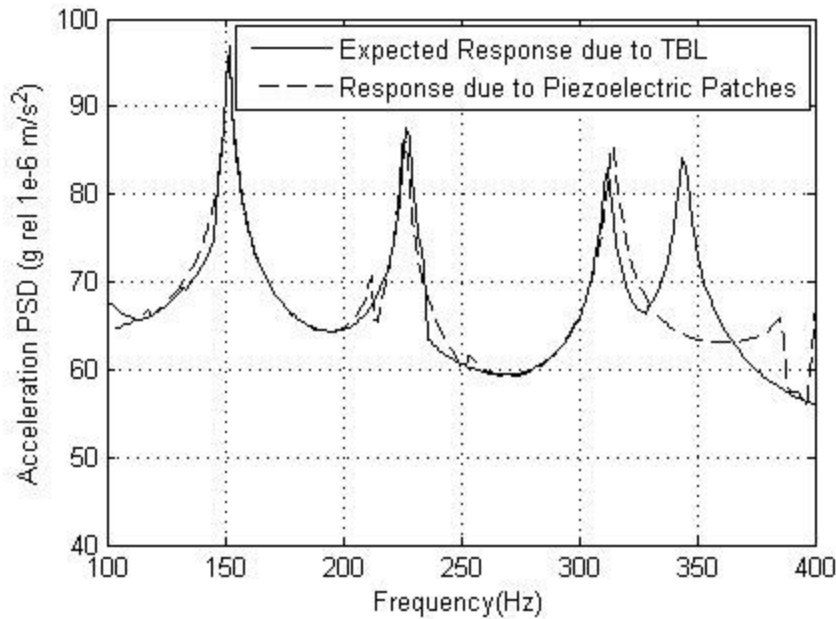


**Figure 31:** Optimal configuration of three piezoelectric patches positions and alternating voltage potentials ( $X1 = 0.3967$  m,  $Y1 = 0.0224$  m,  $\Delta\phi_1^{pZ} = 7.0608$  V,  $X2 = 0.1964$  m,  $Y2 = 0.0283$  m,  $\Delta\phi_2^{pZ} = 2.1062$  V,  $X3 = 0.0439$  m,  $Y3 = 0.0208$  m,  $\Delta\phi_3^{pZ} = 0.0114$  V) to best reproduce the acceleration PSD of a panel caused by the TBL at constant cruise conditions.

It can be seen in Figure 30 and Figure 31 that the addition of each piezoelectric patch allows for one additional panel mode to be reproduced accurately. This shows that the approach of reproducing the panel response from a TBL excitation using piezoelectric patches is a viable option for a select range of frequencies. This approach will work better with smaller piezoelectric patches allowing more patches to be placed on the surface, therefore increasing the frequency range that can be analyzed.

## **Chapter 6: Conclusions and Future Work**

### **6.1 Panel Parameter Optimization**

An optimization study is presented, with the objective of reducing the acceleration PSD of a panel excited by a TBL by optimizing the panel's length. It has been shown that the optimal panel length that results in the true global minimum, follows the same exponential decay as the flexural wavelength, convective wavelength and acoustic wavelength. It has also been shown that at multiples of the optimal panel length, local minimum acceleration PSDs occur. The sensitivity study indicates that panel thickness and panel density are the most consistent and effective parameters at reducing the acceleration PSD, at different octave bands within the human hearing range.

The optimization model described in this thesis will be useful in the early stages of aircraft design to help select panel configurations that reduce the amount of noise due to the TBL inside the cabin of the aircraft.

A next step for this research would be to determine if the optimal panel width is also correlated with the flexural wavelength, convective wavelength and acoustic wavelength. It is of interest to continue the sensitivity study with higher octave bands to determine if panel thickness and density are still the most consistent, and effective parameters at reducing the acceleration PSD.

## **6.2 Experimental Setup**

Two main test setups were used throughout this study to validate the models, and a new test setup was proposed to further research in the field. The NASA test setup was used to compare Rocha's model for a TBL excitation, which was then used to perform the sensitivity study on panel parameters to determine their effect on the acceleration PSD of a panel. The DLR experimental setup was used to compare to Berry's model for both an impact force excitation and a piezoelectric patch excitation. The DLR test setup was used as a guide to design the new test setup at Carleton University which is meant to replicate the effects of a panel with both clamped, and simply supported boundary conditions. This experimental setup still needs validation for the correct boundary conditions. Once the boundary conditions are determined a comparison can be performed to determine which model provides the most accurate prediction of the acceleration PSD caused by different excitations.

## **6.3 Analytical Model Validations for Different Excitations**

The objective of this phase was to validate models of an aircraft panel given different excitations on the panel. The model was given a point force excitation from an impact hammer, a TBL excitation caused by the flow on the outside of the panel, and an excitation from a piezoelectric actuator bonded to the panel. The theoretical values, as predicted by the models, are compared against experimental data from the three excitations.

It has been shown that Berry's modified model can be used to accurately predict a panel's acceleration PSD given a point force excitation, a TBL excitation and a piezoelectric patch excitation over a limited frequency range. Berry's current model has been found to only be valid

for a finite number of panel modes due to the polynomial spatial functions. In the future, other spatial functions might be of interest to investigate in order to determine if a function exists that does not limit the frequency range as significantly. The different excitations have been compared against Ansys, Rocha's model and experimental data.

Since Berry's modified model has been proven to give an accurate prediction of the acceleration PSD for each of the excitations, over a limited frequency range, it can be used to select the optimal positions of piezoelectric patches to reproduce the acceleration PSD caused by a TBL in constant cruise conditions, for the low frequency range. This would allow for cost intensive flight and wind tunnel tests to be reduced, and partially replaced by ground tests using a simple panel/piezoelectric patch experimental setup.

#### **6.4 Piezoelectric Patch Placement Optimization to Reproduce Acceleration PSD for a TBL Excitation**

It has been proven that the addition of each piezoelectric patch allows for one more panel mode to be accurately reproduced. This means that the approach of reproducing the panel response from a TBL excitation using piezoelectric patches is a viable option for a select range of frequencies. This approach will work better with smaller piezoelectric patches allowing more patches to be placed on the surface, therefore increasing the frequency range that can be analyzed.

It would be of interest in future studies to determine if providing the piezoelectric actuators with complex control signals (frequency dependant, for example) would reduce the number of piezoelectric actuators required and/or improve the reproduction of the panel response.

## References

- [1] J. Rocha, A. Suleman, F. Lau, An accurate Coupled Structural- Acoustic Analytical Framework for the Prediction of Random and Flow-Induced Noise in Transport Vehicles: Its Validation, *Can. Acoust.* 37 (2009).
- [2] Laminar to Turbulent Flow, (n.d.). <http://de.swisside.com/wp-content/uploads/2014/05/6-Boundary-Layer-Diagram.jpg> (accessed September 9, 2017).
- [3] Wing Boundary Layer, (n.d.). <http://www.allstar.fiu.edu/aero/images/fig14.gif> (accessed September 9, 2017).
- [4] Aircraft Components and Structure, (n.d.). <http://www.cfinotebook.net/notebook/aerodynamics-and-performance/aircraft-components-and-structure> (accessed September 9, 2017).
- [5] J. Spengler, S. Ludwig, R. Weker, Ozone exposures during trans-continental and trans-pacific flights, *Int. J. Indoor Environ. Heal.* 14 (2004) 67–73.
- [6] T. Lindgren, G. Wieslander, T. Nordquist, B.-G. Dammstrom, D. Norback, Hearing status among cabin crew in a swedish commercial airline company, *Int. Arch. Occup. Environ. Health.* 82 (2009) 887–892.
- [7] W. Gan, H. Davies, P. Demers, Exposure to occupational noise and cardiovascular disease in the United States: the National Health and Nutrition Examination Survey 1999–2004, *Occup. Environmental Med.* 68 (2011) 183–190.
- [8] E. McNeely, S. Gale, I. Tager, L. Kincl, J. Bradley, B. Coull, S. Hecker, The self-reported health of U.S. flight attendants compared to the general population, *Environ. Heal.* 13 (2014) 1–11.
- [9] S.A.J. Sonnenberg, J. Rocha, Extended optimization study and panel parameter study for

- noise radiation reduction of an aircraft panel excited by turbulent flow, *J. Can. Acoust.* 45 (2017) 7–13.
- [10] S.A.J. Sonnenberg, J. Rocha, Optimization study and panel parameter study for noise radiation reduction of an aircraft panel excited by turbulent flow, *J. Can. Acoust.* 44 (2016) 256–257.
- [11] W.A. Strawderman, R.S. Brand, Turbulent-flow-excited vibration of a simply supported, rectangular flate plate, *J. Acoust. Soc. Am.* 45 (1969) 177–192.
- [12] C. Maury, P. Gardonio, S.J. Elliot, A number approach to modelling the response of a randomly excited panel, part i: General theory, *J. Sound Vib.* 252 (2002) 83–113.
- [13] C. Maury, P. Gardonio, S.J. Elliot, A wavenumber approach to modelling the response of a randomly excited panel, part ii: Application to aircraft panels excited by a turbulent boundary layer, *J. Sound Vib.* 252 (2002) 115–139.
- [14] N.H. Schiller, Decentralized control of sound radiation from periodically stiffened panels, Virginia Polytechnic Institute and State University, Blacksburg, Virginia, 2007.
- [15] J.M. Montgomery, Modelling of aircraft structural-acoustic response to complex sources using coupled fem-bem analyses, *Collect. Tech. Pap. - 10th AIAA/CEAS Aeroacoustics Conf.* 1 (2004) 266–274.
- [16] N. Roy, M. Lapi, Efficient Computation of the Radiated Sound Power of Vibrating Structures using a Modal Approach, in: *Acoustics, Paris, 2008*: pp. 381–386.
- [17] J. Rocha, D. Palumbo, On the Sensitivity of Sound Power Radiated by Aircraft Panels to Turbulent Boundary Layer Parameters, *J. Sound Vib.* 331 (2012) 4785–4806.
- [18] J. Rocha, Sound Radiation and Vibration of Composite Panels Excited by Turbulent Flow: Analytical Prediction and Analysis, *Shock Vib.* 2014 (2014) 1–18.

- [19] J. Rocha, A. Suleman, F. Lau, Turbulent Boundary Layer Induced Noise and Vibration of a Multi-Panel Walled Acoustic Enclosure, *Can. Acoust.* 38 (2010) 9–22.
- [20] J. Rocha, A. Suleman, F. Lau, Prediction of Turbulent Boundary Layer Induced Noise in the Cabin of a BWB Aircraft, *Shock Vib.* 19 (2012) 693–705.
- [21] A. Berry, J.-L. Guyader, J. Nicolas, A general formulation for the sound radiation from rectangular, baffled plates with arbitrary boundary conditions, *J. Acoust. Soc. Am.* 88 (1990) 2792–2802.
- [22] F. Charette, F. Berry, C. Guigou, Dynamic Effects of Piezoelectric Actuators on the Vibrational Response of a Plate, *J. Intell. Mater. Syst. Struct.* 8 (1997) 513–524.
- [23] J. Curie, P. Curie, Dilation électrique du quartz, *J. Phys.* 2 (1889) 149–170.
- [24] S. Katzir, *The beginnings of piezoelectricity: a study in mundane physics*, Springer, Dordrecht, 2006.
- [25] M. Karpelson, G.-Y. Wei, R.J. Wood, Driving high voltage piezoelectric actuators in microbotic applications, *Sensors Actuators A Phys.* 176 (2012) 78–89.
- [26] Z. He, H.T. Loh, E.H. Ong, Reliability Evaluation of Piezoelectric Micro-Actuators with Applications in Hard Disk Drives, *IEEE Trans. Magn.* 44 (2008) 3722–3725.
- [27] R.J. Przybyla, S.E. Shelton, A. Guedes, In-Air Ranging With an AIN Piezoelectric Micromachined Ultrasound Transducer, *IEEE Sens. J.* 11 (2011) 2690–2697.
- [28] M. Martins, V. Correia, J.M. Cabral, S. Lanceros-Mendez, J.G. Rocha, Optimization of piezoelectric ultrasound emitter transducers for underwater communications, *Sensors Actuators A Phys.* 184 (2012) 141–148.
- [29] M. Robiony, F. Polini, F. Costa, C. Toro, M. Politi, Ultrasound Piezoelectric Vibrations to Perform Osteotomies in Rhinoplasty, *J. Oral Maxillofac. Surg.* 65 (2007) 1035–1038.

- [30] D.R. Chou, *Piezoelectric Micromachined Ultrasound Transducers for Medical Imaging*, ProQuest Dissertations Publishing, Ann Arbor, 2012.
- [31] A.A. Vives, *Piezoelectric Transducers and Applications*, Springer, New York, 2008.
- [32] G. Caruso, S. Galeani, L. Menini, Active vibration control of an elastic plate using multiple piezoelectric sensors and actuators, *Simul. Model. Pract. Theory*. 11 (2003) 403–419.
- [33] B.-T. Wang, C.R. Fuller, E.K. Dimitriadis, Active control of noise transmission through rectangular plates using multiple piezoelectric or point force actuators, *J. Acoust. Soc. Am.* 90 (1991) 2820–2830.
- [34] J. D’Cruz, Active suppression of aircraft panel vibration with piezoceramic strain actuators, *J. Aircr.* 35 (1998) 139–144.
- [35] C. Maury, S.J. Elliot, P. Gardonio, Turbulent boundary-layer simulation with an array of loudspeakers, *AIAA J.* 42 (2004) 706–713.
- [36] S.J. Elliot, C. Maury, P. Gardonio, The synthesis of spatially correlated random pressure fields, *J. Acoust. Soc. Am.* 117 (2005) 1186–1201.
- [37] T. Bravo, C. Maury, The experimental synthesis of random pressure fields: Methodology, *J. Acoust. Soc. Am.* 120 (2006) 2702–2711.
- [38] C. Maury, T. Bravo, The experimental synthesis of random pressure fields: Practical feasibility, *J. Acoust. Soc. Am.* 120 (2006) 2712–2723.
- [39] M. Aucejo, L. Maxit, J.-L. Guyader, Experimental simulation of turbulent boundary layer induced vibrations by using a synthetic array, *J. Sound Vib.* 331 (2012) 3824–3843.
- [40] O. Robin, A. Berry, S. Moreau, Experimental vibroacoustic testing of plane panels using synthesized random pressure fields, *J. Acoust. Soc. Am.* 135 (2014) 3434–3445.

- [41] M. Misol, S. Algermissen, N. Hu, P. Monner, H, Measurement, simulation and synthesis of turbulent-boundary-layer-induced vibrations of panel structures, in: n.d.
- [42] T. Bravo, C. Maury, A synthesis approach for reproducing the response of aircraft panels to a turbulent boundary layer excitation, *J. Acoust. Soc. Am.* 129 (2011) 143–153.
- [43] J. Ochs, J. Snowdon, Transmissibility across simply supported thin plates. I. Rectangular and square plates with and without damping layers., *J. Acoust. Soc. Am.* 58 (1975) 832–840.
- [44] Y. Champoux, S. Brunet, A. Berry, Champoux, Y, *Exp. Tech.* 20 (1996) 24–26.
- [45] W. Hoppmann, J. Greenspon, An experimental device for obtaining elastic rotational constraints on the boundary of a plate, in: *Natl. Congr. Appl. Mech.*, 1954: pp. 14–18.
- [46] A. Barnard, S. Hambric, Development of a set of structural acoustic teaching demonstrations using a simply-supported panel., in: *Noise-Con*, 2014: pp. 8–10.
- [47] O. Robin, J. Chazot, R. Boulandet, M. Michau, A. Berry, A. Nouredine, A plane and thin panel with representative simply supported boundary conditions for laboratory vibroacoustic tests, *Acta Acust. United with Acust.* 102 (2016) 1–13.
- [48] N. Hu, M. Misol, Effects of riblet surfaces on boundary-layer-induced surface pressure fluctuations and surface vibration, in: *Dtsch. Jahrestagung Fur Akust. Deutsche Gesellschaft Fur Akust.*, 2015: pp. 1–4.
- [49] R.K. Arora, *Optimization: algorithms and applications*, Chapman and Hall, 2015.
- [50] C.S. Beightler, D.J. Wilde, *Foundations of Optimization*, Prentice-Hall, Englewood Cliffs, N.J., 1967.
- [51] U. Diwekar, *Introduction to Applied Optimization*, Springer, New York, 2008.
- [52] J. Nocedal, S.J. Wright, *Numerical Optimization*, Springer, New York, 2006.

- [53] MathWorks, Optimoptions, (n.d.). <https://www.mathworks.com/help/optim/ug/optimoptio> (accessed September 9, 2017).
- [54] MathWorks, Constrained Nonlinear Optimization Algorithms, (n.d.). <http://www.mathworks.com/help/optim/ug/constrained-nonlinear-optimization-algorithms.html#brnox0o> (accessed September 9, 2017).
- [55] L. Yong, Interior Point Algorithms and Applications, *Futur. Intell. Inf. Syst.* (2011) 165–172.
- [56] N. Karmarkar, A new polynomial-time algorithm for linear programming, *Combinatorica.* 4 (1984) 373–395.
- [57] C. Roos, T. Terlaky, J.-P. Vial, *Interior Point Methods for Linear Optimization*, Springer, New York, 2005.
- [58] L. Luksan, C. Matonoha, J. Vlcek, Interior point methods for large-scale nonlinear programming, *Optim. Methods Softw.* 20 (2005) 569–582.
- [59] M.E. El-Hawary, I.A. Farhat, Interior point methods application in optimum operational scheduling of electric power systems, *IET Gener. Transm. Distrib.* 3 (2009) 1020–1029.
- [60] A.D. Nguyen, A. Hachemi, D. Weichert, Applications of the interior-point method to shakedown analysis of pavements, *Int. J. Numer. Methods Eng.* (2008) 414–439.
- [61] S. Granville, J.C.O. Mello, A.C.G. Melo, Application of interior point methods to power flow unsolvability, *IEEE Trans. Power Syst.* 11 (1996) 1096–1103.
- [62] G. Corcos, Resolution of pressure in turbulence, *J. Acoust. Soc. Am.* 35 (1963) 192–199.
- [63] D.M. Efimtsov, Characteristics of the field of turbulent wall pressure fluctuations at large Reynolds numbers, *Sov. Phys. Acoust.* 28 (1982) 289–292.
- [64] C.M. Heatwole, R.J. Bernhard, M.A. Francheck, Robust feedback control of flow induced

structural radiation of sound, 1997.

- [65] R. Rackl, A. Weston, Pressure Flucuation Auto and Cross Spectra Verification and Adjustments Based on TU-144LL Data, NASA CR-213938, Seattle, 2005.
- [66] E.J. Richards, D.J. Mead, Noise and Acoustic Fatigue in Aeronautics, 1968.

# Appendices

## Appendix A - Simply Supported Boundary Condition Test Setup

